Title

Preserved Filamentous Microbial Biosignatures in the Brick Flat Gossan, Iron Mountain, California

Journal

Astrobiology, 15(8)

ISSN

1531-1074

Authors

Williams, Amy J
Sumner, Dawn Y
Alpers, Charles N
et al.

Publication Date

2015-08-01

DOI

10.1089/ast.2014.1235

Peer reviewed

ASTROBIOLOGY
Volume 15, Number 8, 2015

DOI: 10.1089/ast.2014.1235

Preserved Filamentous Microbial Biosignatures in the Brick Flat Gossan, Iron Mountain, California

Amy J. Williams,[1,*] Dawn Y. Sumner,[1] Charles N. Alpers,[2] Suniti Karunatillake,[3] and Beda A. Hofmann[4]

Abstract

A variety of actively precipitating mineral environments preserve morphological evidence of microbial biosignatures. One such environment with preserved microbial biosignatures is the oxidized portion of a massive sulfide deposit, or gossan, such as that at Iron Mountain, California. This gossan may serve as a mineralogical analogue to some ancient martian environments due to the presence of oxidized iron and sulfate species, and minerals that only form in acidic aqueous conditions, in both environments. Evaluating the potential biogenicity of cryptic textures in such martian gossans requires an understanding of how microbial textures form biosignatures on Earth. The iron-oxide-dominated composition and morphology of terrestrial, nonbranching filamentous microbial biosignatures may be distinctive of the underlying formation and preservation processes.

The Iron Mountain gossan consists primarily of ferric oxide (hematite), hydrous ferric oxide (HFO, predominantly goethite), and jarosite group minerals, categorized into *in situ* gossan, and remobilized iron deposits. We interpret HFO filaments, found in both gossan types, as HFO-mineralized microbial filaments based in part on (1) the presence of preserved central filament lumina in smooth HFO mineral filaments that are likely molds of microbial filaments, (2) mineral filament formation in actively precipitating iron-oxide environments, (3) high degrees of mineral filament bending consistent with a flexible microbial filament template, and (4) the presence of bare microbial filaments on gossan rocks. Individual HFO filaments are below the resolution of the Mars Curiosity and Mars 2020 rover cameras, but sinuous filaments forming macroscopic matlike textures are resolvable. If present on Mars, available cameras may resolve these features identified as similar to terrestrial HFO filaments and allow subsequent evaluation for their biogenicity by synthesizing geochemical, mineralogical, and morphological analyses. Sinuous biogenic filaments could be preserved on Mars in an iron-rich environment analogous to Iron Mountain, with the Pahrump Hills region and Hematite Ridge in Gale Crater as tentative possibilities. Key Words: Geobiology—Biosignatures—Filaments—Mars—Microbial fossils. Astrobiology 15, 637–668.

1. Introduction

Recently, the Mars Curiosity rover team identified and characterized a habitable environment in Gale Crater, Mars (Grotzinger *et al.*, 2014; McLennan *et al.*, 2014; Vaniman *et al.*, 2014). The presence of habitable environments on Mars invites questions about the preservation and identification of microbial biosignatures on Mars, if life ever inhabited those environments. To identify microbial biosignatures on Mars, it is crucial to define criteria for potential biosignatures in analogous environments on Earth.

Numerous studies have explored how mineralized biosignatures form and are preserved in iron and silica systems (Juniper and Fouquet, 1988; Cady and Farmer, 1996; Fortin *et al.*, 1997; Hofmann and Farmer, 2000; Banfield *et al.*, 2001; Kennedy *et al.*, 2004; Little *et al.*, 2004; Fortin and Langley, 2005; Hofmann *et al.*, 2008; Parenteau and Cady, 2010; Preston *et al.*, 2011; Peng and Jones, 2012). Filaments composed of minerals have been interpreted as mineral-coated filamentous microbes in a range of environments including hydrothermal veins, volcanic settings, base-metal deposits, and oxidizing ore bodies (Cady and Farmer, 1996;

[1]Department of Earth and Planetary Sciences, University of California, Davis, Davis, California, USA.
[2]U.S. Geological Survey, California Water Science Center, Sacramento, California, USA.
[3]Department of Geology and Geophysics, Louisiana State University, Baton Rouge, Louisiana, USA.
[4]Naturhistorisches Museum der Burgergemeinde Bern, Bern, Switzerland.
*Present address: Center for Research and Exploration in Space Science and Technology, University of Maryland Baltimore County/NASA Goddard Space Flight Center, Greenbelt, Maryland, USA.

Hofmann and Farmer, 2000; Banfield *et al.*, 2001; Jones *et al.*, 2001; Hofmann *et al.*, 2008; Jones, 2010; Preston *et al.*, 2011; Peng and Jones, 2012).

The assertion that Mars likely had environments analogous to terrestrial oxidizing massive sulfide deposits (gossans) (Burns, 1987) is based in part on (1) the presence of komatiitic martian rocks (the terrestrial analogues of which host massive iron sulfides), (2) geochemical and mineralogical similarity to SNC meteorites, and (3) the detection of high iron and sulfur concentrations by X-ray fluorescence on the 1977 Mars Viking lander (Burns and Fisher, 1990a, 1990b). Other studies have also used mineralogy and geochemistry to compare gossans to certain martian environments (West *et al.*, 2009). The potentially widespread presence of oxidized iron and sulfur species on Mars (Lane *et al.*, 2015), the contribution of hydrous iron-sulfates to martian regolith hydration (Karunatillake *et al.*, 2014), and the presence of acid-sulfate weathered outcrops, such as the Burns Formation at Meridiani Planum (Squyres *et al.*, 2004), make terrestrial gossans an appropriate analog environment for biosignature studies relevant to the search for evidence of life on Mars (Sobron and Alpers, 2013; Peterson *et al.*, 2014). An appropriate terrestrial gossan for this analog study is the Iron Mountain massive sulfide deposit and gossan in California.

During weathering of the massive sulfide deposit, the pyrite oxidizes with Fe(III) as the primary oxidant at pH values below 3 (Nordstrom and Alpers, 1999a; Nordstrom, 2003), producing Fe(II), sulfate, and protons. At low pH, the oxidation of Fe(II) to Fe(III) is kinetically limited and proceeds very slowly. However, microbial iron-oxidation dramatically increases the oxidation rate, driving forward the production of more Fe(III) for biotic pyrite oxidation. At slightly less acidic pH vales, the precipitation of Fe(III) minerals can drive forward the production of more acidity (Baker and Banfield, 2003; Nordstrom, 2003) and precipitate a variety of Fe(III) minerals. Poorly crystalline iron-oxide phases precipitate first, such as hydrous ferric oxides (HFOs), ferrihydrite ($(Fe^{3+})_2O_3 \cdot 0.5H_2O$), schwertmannite ($Fe_8O_8(OH)_6SO_4$), and jarosite group minerals ($MFe_3(OH)_6(SO_4)_2$), where M is a cation, most commonly K^+ but also possibly Na^+ or H_3O^+ (Velasco *et al.*, 2013). Several of these will transform to more ordered crystalline phases, such as ferric oxide (hematite, Fe_2O_3), goethite (α-FeO(OH)), and lepidocrocite (γ-FeO(OH)). The pH and Eh of these acid drainage waters control aqueous iron speciation and the iron and sulfate minerals that precipitate from solution. These iron precipitates are themselves a biosignature. They also coat objects, including microbial filaments, to form HFO filament casts of the microbial structures. Where microbial filaments are no longer present, but HFO filament casts of microbial filaments are preserved, the composition and morphology of these HFO filaments may serve as biosignatures.

The Iron Mountain massive sulfide deposit (Kinkel *et al.*, 1956; Albers, 1985; Albers and Bain, 1985; Alpers *et al.*, 2003) is a compelling site at which to investigate the formation and preservation of mineralized filamentous microbial biosignatures within the context of mineralogical, textural, and geochemical characteristics of the gossan. The gossan consists predominantly of HFO, which is the primary component of HFO filaments in the gossan. The processes that form these filaments lead to specific compositional and morphological features that indicate the former presence of microbial filaments. Here, we use a suite of techniques to evaluate the processes that lead to HFO filament formation and preservation. We also evaluate the potential of HFO filaments within the Iron Mountain gossan to represent a biosignature and the implications for biosignature detection on Mars, specifically with the instruments on board Curiosity. Mineral filament structures could be identified on Mars as similar to filamentous microbial biosignatures on Earth by using the suite of analytical instruments on Curiosity to define the geochemistry and mineralogy of a specific martian environment. The collective insight from mineralogy, chemistry, and morphology can also constrain the formation and preservation models for putative martian biosignatures, as applied by Fru *et al.* (2013) to ancient terrestrial environments. Recently, the Curiosity rover encountered a region affected by acid-sulfate weathering at the Pahrump Hills region in Gale Crater (Cavanagh *et al.*, 2015; Farmer *et al.*, 2015; McAdam *et al.*, 2015). Another iron-bearing environment appropriate for biosignature preservation that Curiosity would investigate is the hematite-bearing ridge on Mt. Sharp in Gale Crater (Fraeman *et al.*, 2013). Although Fraeman *et al.* (2013) did not consider an Fe-sulfide progenitor for the hematite ridge, the use of gossans to approximate the mineralogy of an iron-oxide-bearing formation such as the hematite ridge is reasonable. While low-pH minerals such as jarosite have not been identified from CRISM data at the hematite ridge, jarosite has been found by Curiosity in other hematite-rich environments (where jarosite was also not identified) as detected with CRISM, such as Pahrump Hills (Cavanagh *et al.*, 2015).

2. Background

2.1. Iron Mountain

Iron Mountain, California (Fig. 1), contains a well-preserved, laterally discontinuous gossan cap formed from an oxidized massive sulfide deposit. The dearth of clastic sediment in the host rock and the low Pb content suggests that the Iron Mountain deposit shares characteristics with both the ''type 1'' volcanogenic massive sulfide deposits of Franklin *et al.* (1998) and the bimodal mafic category of Barrie and Hannington (2000). Both of these deposit types are associated with arc-related rifts (Alpers *et al.*, 2003). The Iron Mountain volcanogenic massive sulfide deposit formed in a Devonian marine island-arc setting characterized by an extensional, graben-like environment (Albers and Bain, 1985). In this extensional environment, the massive sulfide bodies were emplaced in the Copley Greenstone formation and the middle unit of the Balaklala Rhyolite, and were syngenetic with the formation of these host rocks (Albers and Bain, 1985). The mafic flows and pyroclastic deposits constitute the Copley Greenstone, which is interpreted to have formed subaqueously (Kinkel *et al.*, 1956).

Eruption of Balaklala rhyolitic lavas coincided with the end of the Copley mafic lava eruptions, and although mafic and rhyolitic units overlapped in some areas, boundaries between the mafic and rhyolitic flows were well-defined (Kinkel *et al.*, 1956). The Balaklala Rhyolite was deposited in both subaqueous and subaerial environments. The Copley Greenstone and Balaklala Rhyolite were overlain by a series

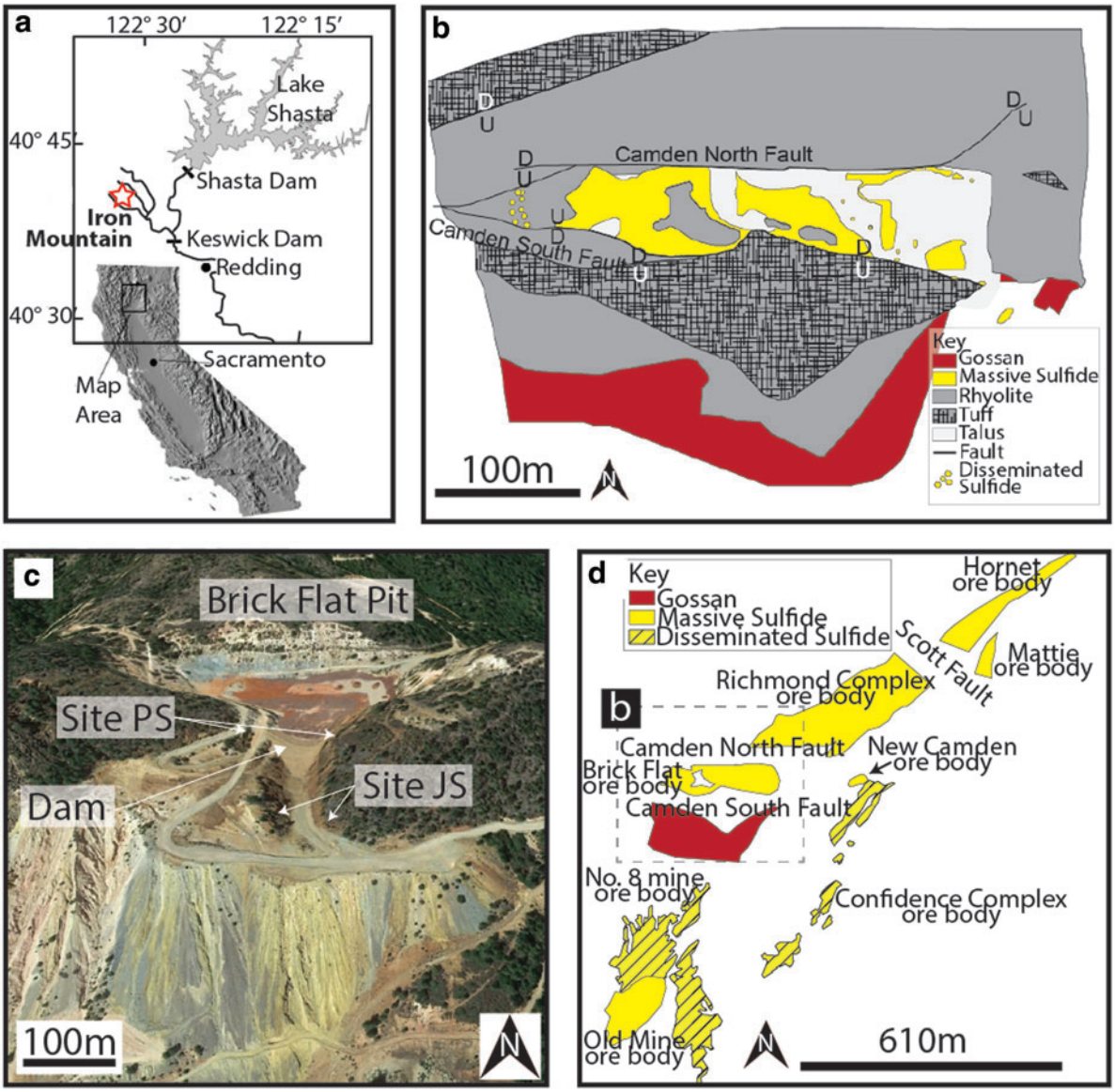

FIG. 1. Local map, geological map, and sample sites from the Iron Mountain Brick Flat pit gossan. (**a**) Map showing the location of Iron Mountain in California (modified from Alpers *et al.*, 2003). (**b**) Geological map of the Brick Flat massive sulfide deposit (modified from Albers, 1985). (**c**) Oblique view of sample sites PS and JS relative to the Brick Flat pit. Base image from GoogleEarth. (**d**) Map showing the location of the Brick Flat massive sulfide deposit relative to the other Iron Mountain cluster sulfide bodies (modified from Albers, 1985). The outlines of ore bodies are at different depths and are projected. Dashed box indicates the location of (b). The Okosh and Busy Bee ore bodies are not shown. (Color graphics available at www.liebertonline.com/ast)

of volcanic, volcaniclastic, clastic, and carbonate rock units younger than Jurassic (Albers and Bain, 1985). All units older than Late Jurassic, including the Balaklala Rhyolite and associated massive sulfides (Fig. 1), were exposed to varying degrees of metamorphism and hydrothermal alteration during submarine burial and subsequent oceanic crust accretion onto the continent (Alpers *et al.*, 2003).

Formation of the massive sulfide deposits in the West Shasta mining district, including the Iron Mountain ore bodies, proceeded through several stages. In the first stage, the hypogene/subsurface pyrite formed syngenetically with the middle unit of the Balaklala Rhyolite in an extensional, graben-like environment (Albers, 1985). Pyrite emplacement was followed sequentially by chalcopyrite, quartz, sphalerite, and calcite precipitation. During pyrite formation, a network of quartz, sericite, and illite crystals that formed around the pyrite grains was interpreted to represent recrystallized host rock material, related to regional metamorphism and hydrothermal alteration (Kinkel *et al.*, 1956). Some of the quartz may also be secondary. The final supergene (near-surface) stage consisted of oxidation and enrichment of mineral deposits. The timing of supergene enrichment and gossan formation is unknown but likely began prior to 780,000 years before present based on reversed magnetism in part of the gossan (Alpers *et al.*, 1999). The only supergene metal element enrichment observed at

Iron Mountain was copper in the Old Mine and Richmond ore bodies (Fig. 1d; Kinkel *et al.*, 1956).

At Iron Mountain, iron sulfides most commonly occur as massive sulfide deposits and less frequently as disseminated pyrite deposits (only near the No. 8 Mine; Fig. 1d). The Iron Mountain ore deposit cluster is composed of eight known ore bodies. Five of these ore bodies originally formed a single, continuous deposit, which was fractured subsequently by Late Jurassic orogenic faulting (Kinkel *et al.*, 1956; Albers, 1985). The five fractured ore bodies (Hornet, Richmond, Complex, New Camden, and Brick Flat) are separated by the Scott and Camden faults. Regional compression and uplift along these faults exposed some ore bodies to weathering and erosion, including Brick Flat. Regional faults, including the North and South Camden faults that fracture Brick Flat, facilitated supergene alteration and subterranean sulfide oxidation caused by percolation of groundwater recharged by precipitation; oxidation has been documented to a depth of ~122 m along the Camden fault footwall (Kinkel *et al.*, 1956).

Iron Mountain gossan rocks have been differentiated into two groups based on original pyrite content (Kinkel *et al.*, 1956). The first group formed from disseminated pyrite and varies from scattered pyrite pseudomorphs in a host-rock matrix to a rock-and-silica sponge texture that contained >50% pyrite. The second group formed from massive pyrite and consists of earthy, cellular, or spongy masses of iron oxides coating quartz septa, iron-oxide crusts, or a breccia of remobilized angular rock and quartz fragments in an iron-oxide matrix (Kinkel *et al.*, 1956).

2.2. Brick Flat gossan at Iron Mountain

Before the Brick Flat massive sulfide deposit was first oxidized, the rocks were principally composed of pyrite with a quartz boxwork that filled in between pyrite crystals and crosscut structurally weak zones in the massive pyrite (Kinkel *et al.*, 1956). Exposure to water and oxygen over geological time oxidized the pyrite, releasing oxidized iron and sulfur species, as well as acidity due to proton production, to the environment. The gossan and associated oxidized iron and sulfur species extend *ca.* 40 m into the subsurface (Albers, 1985), with a documented maximum depth ~122 m (Kinkel *et al.*, 1956).

Recent mining of Brick Flat (1860s to 1960s) exposed additional pyrite, leading to accelerated pyrite oxidation. After pyrite oxidation, negative pyrite pseudomorphs were preserved in the quartz boxwork. The region where the oxidized iron precipitated, both within and on the quartz boxwork, is defined here as the *in situ* gossan.

During and after weathering of the massive sulfide, ferrous iron (Fe(II)) was mobilized from pyrite into aqueous fluids due in large part to the biotic oxidation of sulfide minerals. The iron oxidized to ferric (Fe(III)) and, under appropriate geochemical conditions, precipitated from these fluids onto the substrate. In this manner, iron-rich ''remobilized'' rock masses formed, overlying *in situ* gossan rocks. These masses formed a variety of spatially restricted, iron-rich deposits. Because the iron oxidation was mostly biotic, the presence of these iron precipitates is in and of itself a biosignature. The iron-oxide precipitates coated both large surfaces and small features, including microbial filaments, which can serve as micro- to macroscale biosignatures.

Table 1. Gossan Sample Names, Figures, and Locations

Site	*Sample ID*	*Related figure*	*Latitude*	*Longitude*
PS				
	PS1	Fig. 2d, Fig. 11b, 11d	40.674045°	-122.528237°
	PS3	Fig. 2g, Fig. 4, 5, 6, 7, 8	40.674288°	-122.528435°
	PS8	Fig. 2l	40.674034°	-122.528467°
	PS9	Fig. 2l	40.674034°	-122.528467°
	PS16	Fig. 2i	40.674232°	-122.527185°
	PS18	Fig. 2j	40.674232°	-122.527185°
JS				
	JS1	Fig. 2k	40.673086°	-122.527334°
	JS3	Fig. 2c, Fig. 3	40.673086°	-122.527334°
	JS4	Fig. 2n, Fig. 10	40.673139°	-122.527789°
	JS17	Fig. 2m	40.672705°	-122.527116°
	JS18	Fig. 2d	40.672705°	-122.527116°

Latitude and longitude reported in NAD83.

Samples described here were from gossan associated with massive pyrite of the Brick Flat deposit. This low-copper, pyritic deposit was mined from the mid-1950s to 1962 as a source of sulfur for sulfuric acid production (Albers, 1985). Mining activity exacerbated oxidative pressure, as adits provided additional avenues for water and oxygen to interact with fresh pyrite and produce acid mine drainage (Alpers *et al.*, 2003). The top of the western third of the deposit was not mined and remains intact. The bottom of the deposit is not exposed; cores from below the sulfide deposit were described as a pyritic stockwork with quartz or heavily pyritized rhyolite (Albers, 1985). The Brick Flat deposit offers a window into surficial oxidation of massive sulfide at Iron Mountain.

2.3. Field sites

Gossan and pyrite samples were collected from the Brick Flat pit (Fig. 1). Samples labeled PS were collected from (1) a road cut southwest of the Brick Flat pit and (2) the eastern side of the pit retention dam (Table 1). Samples labeled JS were collected from (1) the gossan walls below the retention dam and (2) along the road southeast of the pit and parallel to the cliff (Table 1).

3. Methods

Samples of pyrite and quartz boxwork (PQB) from the *in situ* gossan, HFO and quartz boxwork (QBG) from the *in situ* gossan, and iron-only (IO) gossan rock from remobilized iron deposits were characterized with a suite of optical, mineralogical, and chemical techniques. These analytical techniques were utilized to characterize the mineralogy and mineral morphology of the gossan samples and determine the biogenicity of HFO filaments.

3.1. Mineral and chemical analyses

The bulk mineralogical composition of the PQB, QBG, and IO samples was determined on powdered samples with

a Rigaku Ultima IV X-ray diffractometer with a Cu Kα radiation source. Samples were scanned from 2° to 64° 2θ. The measured patterns were then compared to standard mineral spectra from the RRuff repository (Downs, 2006) and to International Centre for Diffraction Data (ICDD) files using PDXL software to characterize the sample mineralogy. Analyses were conducted in the Southard Lab in the Department of Land, Air, and Water Resources at University of California (UC), Davis.

Iron-sulfate salts and (hydrous) ferric oxides were identified in the gossan. Most phases were identified using X-ray diffraction (XRD), although several trace mineral phases were identified by energy-dispersive spectroscopy (EDS) and based on morphology from scanning electron microscopy (SEM) images (see Section 4.1.1). Minerals identified by SEM included halotrichite group minerals, copiapite group minerals, and a silver- and sulfur-bearing mineral. These minerals were identified by comparing their EDS spectra and morphology in SEM images to the crystal structure of iron-sulfate salts identified in other acid drainage environments (*e.g.*, Hammarstrom *et al.*, 2005; Gomes and Favas, 2006; Abdel-Aal and Farghaly, 2007; Murgida and Hildebrandt, 2008; Panneerselvam *et al.*, 2008). Secondary sulfate minerals have been documented in a variety of acid drainage systems (*e.g.*, Hammarstrom *et al.*, 2005). For example, halotrichite group minerals at Iron Mountain gossan were identified by comparing the mineral morphology to secondary sulfate salts identified by Hammarstrom *et al.* (2005). EDS spectra were then used to confirm the halotrichite group mineral identification at Iron Mountain.

3.2. Imaging

Freshly broken and naturally weathered sample surfaces were imaged with SEM at various resolutions with both secondary electron (SE) and backscatter electron (BSE) imaging techniques. Mineral morphologies were visualized at up to 2000× resolution with a Hitachi TM3000 tabletop scanning electron microscope in the Earth and Planetary Sciences Department at UC Davis. This was followed by up to 50,000× magnification imaging with the Philips XL30S field emission gun (FEG) scanning electron microscope with a Phoenix amplifier energy-dispersive X-ray (EDAX) spectroscopy system and a SUTW Si (Li) detector in the Advanced Material Characterization and Testing Laboratory at UC Davis. Select adjacent SEM images were stitched together into mosaics with Adobe Photoshop CS3 mosaic software.

3.3. Hydrous ferric oxide filament morphology quantification

Hydrous ferric oxide filament morphology was quantified by using the methods of Hofmann *et al.* (2008). Four morphological parameters (defined below) of HFO filaments, microbial filaments, and abiotic mineral fibers were measured in SEM images. The morphological parameters measured were (1) filament or fiber diameter, (2) tortuosity, (3) bending (degrees/20 μm), and (4) number of direction changes/20 μm. These parameters were measured on (1) microbial and mineral filaments from Iron Mountain and (2) microbial filaments from the literature: three Iron Mountain gossan samples with microbial filaments ($N=20$ microbial filaments), seven examples of microbial filaments from the literature (Seeger and Jerez, 1993; Schrenk *et al.*, 1998; Edwards *et al.*, 1999; Gumaelius *et al.*, 2001; Schieber and Glamoclija, 2007; Florea *et al.*, 2011; Preston *et al.*, 2011) ($N=22$ microbial filaments), one halotrichite group mineral salt sample from Iron Mountain ($N=10$ fibers), one Iron Mountain sample with cryptic filaments ($N=12$ cryptic filaments), one Iron Mountain sample with central filament lumina ($N=6$ lumina), and eight Iron Mountain samples with HFO filaments ($N=318$ HFO mineral filaments).

Morphologies were measured on digital images of HFO filaments, microbial filaments, and mineral fibers using the National Institutes of Health software ImageJ. Each filament or fiber was traced along one side of its outside perimeter as a series of line segments, and the data points were exported as XY coordinates in a text file. Then filament diameter and straight length were measured separately, and tortuosity, bending, and number of direction changes per unit length were calculated from this data for each filament. Tortuosity was defined as the length of the filament divided by the shortest distance between its ends. Bending was defined as the sum of the absolute value of the degrees the filament bends between each line segment, divided over the total filament length. Substantial bending in and out of the XY measurement plane could skew the measurement results. Therefore, only filaments that appeared to be mostly in the plane of the image were measured. Almost all the filaments were in the measurement plane in the SEM mosaics, such that larger filament fragments were not artificially excluded. We defined the number of direction changes as the number of times the traced line segment entered one of four quadrants in a Cartesian plane (or, whether each XY coordinate along the traced line entered a different quadrant relative to the previous XY coordinate). To compare the number of direction changes and extent of bending among fibers and filaments of various origins, the number of direction changes and bending were normalized to the mean length of the shortest fibers. These had a mean fiber length of 20 μm. In contrast, the average measured length of filaments was >100 μm, and both ends of some filaments were not observed. The order-of-magnitude difference in length required normalization to allow comparisons of geometry. Thus, the bending and number of direction changes reported are considered the minimum value for each morphology parameter, as filaments were longer than the scanning electron microscope field of view, and any additional bending and direction changes along the filament were not accounted for in the measurement.

We assessed pairwise distinctness to determine whether microbial filaments are morphologically more distinct from smooth HFO filaments, bumpy HFO filaments, cryptic filaments, and mineral fibers than these HFO filament and fiber types are from each other. A modified version of the methods by Karunatillake *et al.* (2011) was utilized, with the detailed analytical Mathematica file included in the Supplementary Material (available online at www.liebertonline.com/ast). In this approach, we quantified the likelihood that two pseudo-random samples (biogenic-abiogenic, biogenic-unknown, abiogenic-unknown, unknown-unknown) from the same parent Gaussian distribution could differ in their mean values by at least as much as the observed. This uses Eqs. 19 and 20 of Section 5.1.1 in the supplement by

Karunatillake *et al.* (2011). Consequently, higher probabilities support the null hypothesis that the samples derive from the same distribution, while lower stochastics would negate the null hypothesis. Accordingly, we label this the ''improbability of pairwise distinctness,'' with lower values conferring a greater confidence that the two samples represent distinct distributions.

4. Results

Gossan samples were divided into three major rock types: pyrite and quartz boxwork (PQB) rock, HFO and quartz boxwork gossan (QBG), and iron-only (IO) gossan rock (Table 2). Quartz boxwork texture is defined by quartz septa—partitions composed of quartz that originally separated pyrite crystals. In the PQB rocks, the septa surrounded individual pyrite grains or areas of massive pyrite. Individual septa were spaced <1 mm to ≥13 mm from each other. In the QBG rocks, the septa outlined small to medium (<1 mm to ≥13 mm) negative pseudomorphs of pyrite. In both rock types, septa intersected at irregular angles and formed a larger boxwork texture (Blanchard, 1968; Taylor, 2011).

These major rock types contained a variety of outcrop-scale features, including pyrite (and jarosite group minerals) in altered rhyolite, quartz boxwork with HFO, and HFO-dominated rocks without quartz boxwork. The various abiotic and biotic features in the samples described below hold clues to assess the biogenicity of filamentous features and understand biosignature formation in the context of diverse mineral textures and larger-scale environments.

4.1. In situ *gossan—quartz boxwork and pyrite*

The host rock in the Brick Flat surface *in situ* gossan is a medium- to coarse-grained rhyolite (Albers, 1985). Much of the rhyolite was altered and bleached white, making it friable. Quartz boxwork within the altered rhyolite hosted the sulfide minerals, which were dominated by pyrite in these samples. Pyrite was massive to very fine-grained with rare, small brassy-yellow, subhedral to euhedral crystals. Some samples also contained jarosite group minerals, which led to subdivision of samples into two classes: pyrite with quartz boxwork in altered rhyolite, and pyrite with quartz boxwork and jarosite group minerals in altered rhyolite.

Pyrite with quartz boxwork formed areas centimeters to decimeters in diameter in altered rhyolite outcrop. Pyrite concentrations ranged in size and shape from large blocks of massive, gray pyrite (tens of millimeters in diameter) to stringy veins (~1 mm wide, tens of millimeters long, several millimeters thick; Fig. 2a). All these pyrite-dominated regions are described below as *blebs:* irregularly shaped inclusions within a larger zone of differing mineralogy (commonly goethite here). In hand sample, areas of pyrite with quartz boxwork were separated from each other by centimeters of altered rhyolite (Fig. 2a). The contact between pyrite and rhyolite was rounded to subangular. Some pyrite blebs were separated from the altered rhyolite by regions of bare quartz boxwork (1–3 mm thick) with pores <1 to 3 mm in width defined by septa. In other instances, the boundary between the pyrite and altered rhyolite occurred within micrometers, or the two phases touched. Isolated crystals of pyrite were rarely observed.

Pyrite with quartz boxwork and jarosite group minerals formed areas tens of centimeters wide and tall in altered rhyolite outcrop. In hand sample, orange-yellow jarosite (identified with XRD) was present on the exposed surface of the altered rhyolite and formed a veneer several millimeters thick (Fig. 2b). Little to no jarosite was present on the pyrite. The jarosite deposits were separated by centimeters from each other by blocks to stringy veins of pyrite, described above. The contact between jarosite/rhyolite and pyrite was rounded to subangular.

TABLE 2. MAJOR GOSSAN ROCK TYPES AND ASSOCIATED HAND SAMPLE–SCALE AND MICROSCALE TEXTURES

Major rock type	*Hand sample–scale textures*	*Microscale textures*
PQB Pyrite and quartz boxwork rock (from the *in situ* gossan) ~pH 2.5–3	• Pyrite with quartz boxwork in altered rhyolite • Pyrite with quartz boxwork and jarosite in altered rhyolite	• White tabular crystals • Fibrous efflorescent crystals • Cryptic filaments • Coupled oblong spheroids
QBG HFO and quartz boxwork gossan rock (from the *in situ* gossan) ~pH 5.5–6	• Dull luster QBG • Brightly colored QBG • Resinous luster QBG	• Bumpy HFO filaments • Hexagonal plates • Oblate spheroids • Laminated HFO (hemi)spheres • Smooth spheres • Bladed crystals • Tabular crystals • Knurled surfaces • Hatched surfaces • Agglomerated anhedral crystals
IO Iron-only Gossan rock (from the remobilized iron deposits) ~pH 5.5–6	• Brightly colored laminated HFO • Dull laminated HFO • Dendritic HFO masses • Coalesced vertical columns • Siliceous HFO masses • Clast- and HFO filament–bearing masses	• Smooth HFO filaments • Patterned HFO masses • Laminated HFO masses • Coupled oblong spheroids • Filamentous plexi • Mats of organic filaments • Bundled filament networks

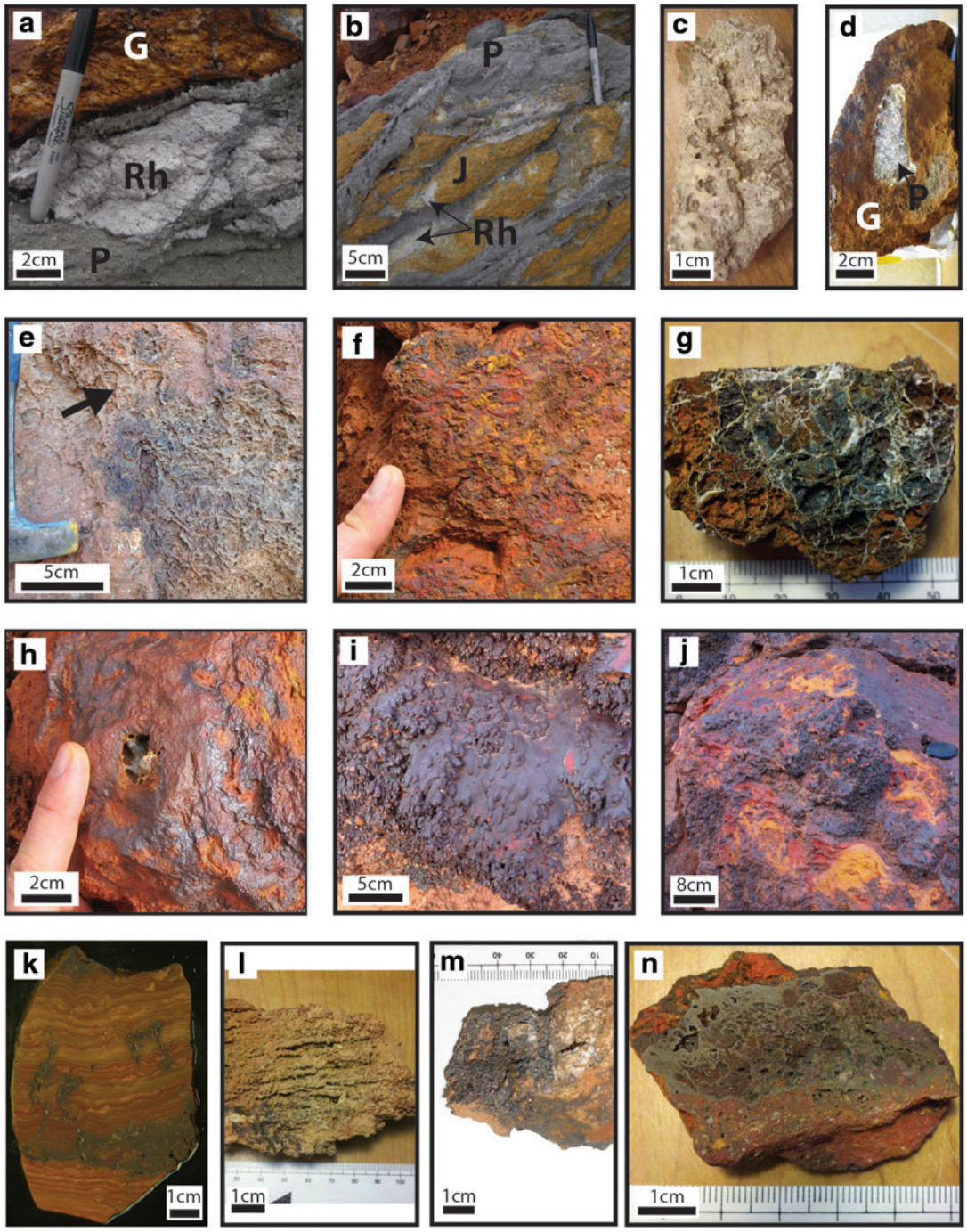

FIG. 2. Gossan (G) rock textures. Characterized rock textures are divided into three groups: pyrite-dominated (PQB), quartz boxwork and HFO rocks (QBG), and iron-only (IO) rocks. PQB rocks include (**a**) pyrite (P) in altered rhyolite (Rh), (**b**) pyrite and jarosite group minerals (J) on altered rhyolite, and (**c**) pyrite with sulfate salts (including copiapite and halotrichite group minerals). QBG rocks include (**d**) HFO (G) with pyrite, (**e**) dull luster QBG, (**f**) brightly colored QBG, (**g**) broken-face interior of QBG, and (**h**) resinous luster QBG. IO rocks include (**i**) dendritic HFO masses (this IO rock is shown overlapping the dull luster QBG rock), (**j**) brightly colored laminated HFO, (**k**) dull laminated HFO, (**l**) coalesced vertical columns of HFO, (**m**) siliceous HFO mass, and (**n**) clast- and HFO-filament-bearing HFO masses. (Color graphics available at www.liebertonline.com/ast)

4.1.1. Description of microscale iron-sulfate salt morphology. A variety of iron-sulfate salts formed micrometer- to millimeter-scale deposits on the pyrite. Salts identified with only XRD included coquimbite, rozenite, rhomboclase, and jarosite group minerals. Salts identified via morphology in SEM images and EDS included copiapite group minerals (white tabular crystals) and halotrichite group minerals (fibrous efflorescent crystals) (Table 3). Copiapite group minerals are described in the Supplementary Material.

Table 3. Identified Gossan Minerals

Mineral	Idealized formula	Identification method		
		Reflected light microscopy	*XRD*	*SEM (mineral morphology, EDS)*
Hematite	Fe_2O_3	X		
Quartz	α-SiO_2	X	X	X
Pyrite	FeS_2	X	X	X
Goethite	α-FeO(OH)	X	X	X
Jarosite group minerals	$(K,Na,H_3O)Fe^{3+}{}_3(SO_4)_2(OH)_6$		X	
Rozenite	$Fe^{2+}SO_4 \cdot 4H_2O$		X	
Coquimbite	$Fe_2{}^{3+}(SO_4)_3 \cdot 9H_2O$		X	
Rhomboclase	$(H_3O)Fe^{3+}(SO_4)_2 \cdot 3H_2O$		X	
Acanthite (?)	Ag_2S			X
Halotrichite group minerals	$(Fe^{2+},Mg^{2+})(Al^{3+},Fe^{3+})_2(SO_4)_4 \cdot 22H_2O$			X
Copiapite group minerals	$(Fe^{2+},Mg^{2+},0.67Fe^{3+},0.67Al^{3+})$ $Fe^{3+}{}_4(SO_4)_6(OH)_2 \cdot 20H_2O$			X

Fibrous efflorescent crystals: Fibrous efflorescent crystals formed bundles that were spaced on pyrite surfaces from tens of micrometers to several millimeters apart (Fig. 3c, 3d). The bundles were 50–100 μm long, 15–50 μm wide, and exhibited Fe, Al, and S peaks in EDS spectra. Bundles were composed of tens to hundreds of crystals. Individual crystals ranged from 6.9 to 28.4 μm long and 1.7 μm in diameter on average ($N = 10$, range = 0.6–6.9 μm). Individual fibrous crystals either maintained a uniform diameter along the fiber or achieved their greatest thickness in the middle of the fiber, with tapering along the fiber length.

4.1.2. Description of microscale cryptic filament mineral morphology. *Cryptic filaments:* Cryptic filaments were present attached to and entwined in fibrous efflorescent salt crystals (Fig. 3d) and spanned voids between individual fibrous efflorescent salt crystals. Cryptic filaments exhibited a similar average atomic weight and, therefore, shade of gray in backscatter SEM images as the fibrous efflorescent salt crystals. Individual cryptic filaments averaged 0.5 μm in diameter (range = 0.2–0.7 μm, $N = 12$) and ranged from 7.3 to 21.9 μm long, although they were likely longer, given often-concealed filament ends. Individual cryptic filaments maintained a uniform diameter along their length. Individual cryptic filaments had a greater degree of bending (average = 126°/μm) than adjacent fibrous efflorescent salt crystals (average = 16°/μm).

4.2. In situ *gossan—HFO and quartz boxwork*

The second type of *in situ* gossan rock is composed of HFO and quartz boxwork. These rocks consisted of quartz boxwork septa coated by laminated to colloform HFO. Isolated blebs of pyrite were also present locally. Samples that lacked pyrite had a dull or resinous luster, and some samples were brightly colored (Supplementary Material). Certain subtypes of this rock contained characteristic mineralized filamentous features coated in submicrometer HFO particles that were interpreted as filamentous microbial biosignatures, while other subtypes contained a variety of euhedral mineral morphologies, consistent with abiotic mineral precipitates, which often overgrew mineralized filamentous features in boxwork voids. The detailed descriptions (below) of these different features contributed to the identification of filamentous microbial biosignatures in the *in situ* gossan. By characterizing the variety of mineral morphologies present in the HFO and quartz boxwork rocks, those morphologies that were biogenically influenced were identified.

4.2.1. Description of microscale mineral morphology. Hydrous ferric oxides coated the quartz boxwork (Fig. 4a, 4b) and formed varied mineral morphologies, including bumpy-surface HFO filaments, hexagonal plates (Supplementary Material), oblate spheroids, laminated HFO (hemi) spheres (Supplementary Material), smooth spheres, bladed crystals, tabular crystals (Supplementary Material), knurled surfaces (Supplementary Material), hatched surfaces, and agglomerated anhedral crystals (Supplementary Material). This variety of morphologies and textures was composed only of HFO. The knurled and hatched surfaces were expressions of the geometry of the HFO filaments, spheres, spheroids, and tabular and bladed crystals where they were very closely spaced.

Bumpy HFO filaments: Tens to hundreds of bumpy (an uneven surface with elevated and depressed regions) HFO filaments formed a networklike structure of overlapping filaments present throughout QBG rock voids, encompassing areas of thousands of cubic micrometers (Fig. 5b). Filaments ranged from touching to spaced tens of micrometers apart, and they often extended into void space unsupported on one end of the filament. They were not observed attached directly to the quartz boxwork surface, but any attachment to quartz boxwork may have been obscured by other HFO minerals that covered the HFO filament attachment points. Bumpy HFO filaments intersected at angles ranging from subparallel to perpendicular. At intersections, the filament diameter sometimes increased at the juncture then decreased in diameter to a size consistent with the pre-intersection diameter. Filaments averaged 9.8 μm in diameter (range = 2.4–31.8 μm, $N = 191$ filaments) and averaged 109 μm in length (range 12.6–563.7 μm), although some filaments were likely longer as not all the filament ends were exposed. Individual filaments were curvilinear and cylindrical, did

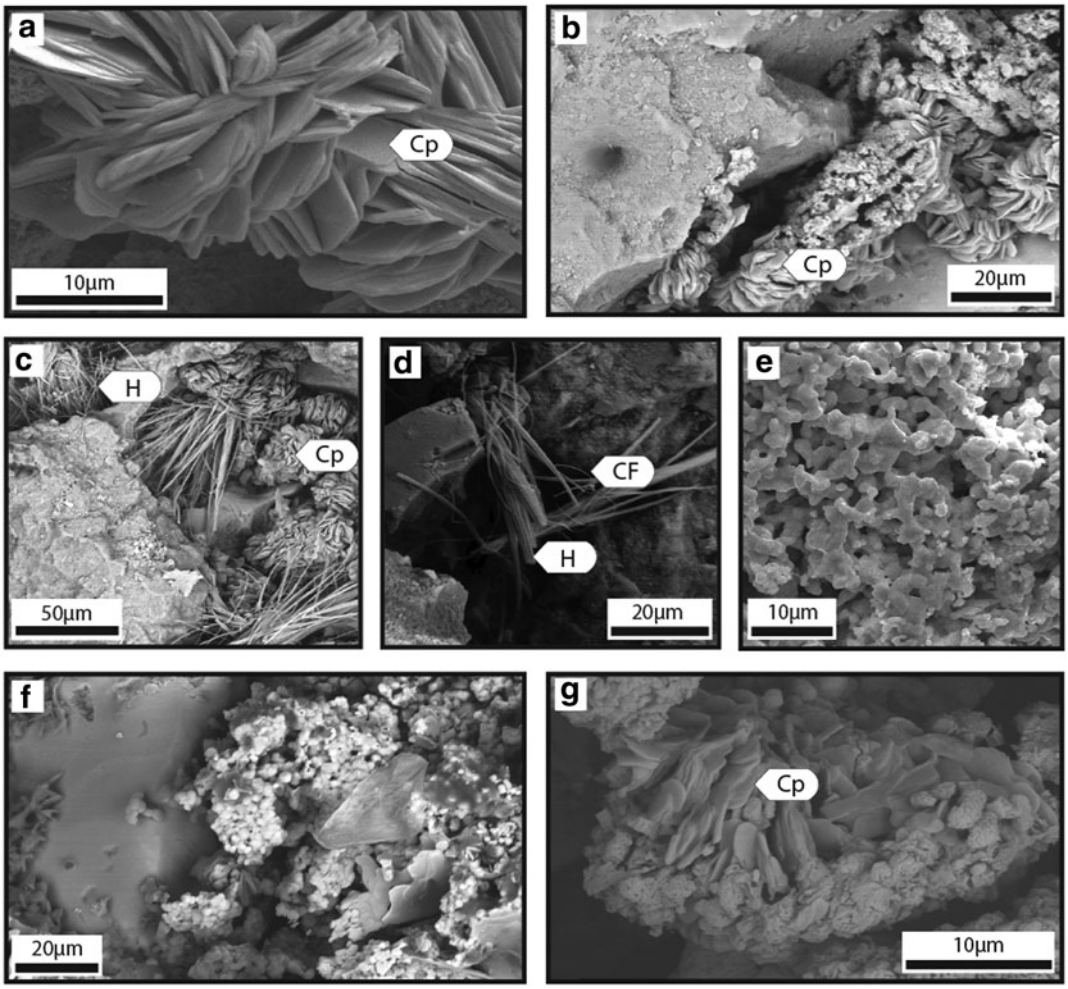

FIG. 3. Iron-sulfate efflorescent salts on PQB rocks. All images were acquired with FEG-SEM. (**a**) SE image of tabular polygonal crystals identified as copiapite (Cp) group minerals by mineral morphology, (**b**) BSE image of tabular polygonal copiapite group mineral crystals associated with unidentified efflorescent iron-sulfate salts, (**c**) BSE image of bundled fibrous crystals of halotrichite (H) group minerals, identified by their distinct mineral morphology, are associated with euhedral crystals likely of copiapite group minerals. (**d**) BSE image of fibrous crystals of halotrichite group minerals and cryptic filaments (CF), (**e**) SE image of anhedral crystals of cemented silver- and sulfur-bearing particles, (**f**) BSE image of small (average = 2.3 μm; $N = 20$) smooth spheres of unidentified iron-sulfate salts in association with pyrite, (**g**) BSE image of tabular, polygonal copiapite group minerals associated with unidentified iron-sulfate salts.

not branch, and had generally uniform diameters. Individual filaments were composed of submicrometer HFO particles that formed a bumpy surface expression. Other HFO mineral morphologies, such as smooth spheres, bladed crystals, and hatched surfaces (described below) were frequently on top of and surrounding bumpy HFO filaments.

Oblate spheroids: The space between oblate spheroid masses ranged from zero (touching) to tens of micrometers apart on quartz boxwork septa in QBG rock voids (Fig. 6d). The oblate spheroid masses were present throughout QBG rock voids, encompassing areas of thousands of cubic micrometers. Oblate spheroids were attached to laminated HFO (hemi)spheres and knurled surfaces. Oblate spheroids formed both agglomerations and chain structures but did not form long, curvilinear, self-supported structures like the bumpy HFO filaments. Agglomerations (Fig. 6e, 6h) were present as hundreds to thousands of oblate spheroids connected to each other at several points (Fig. 6d, 6g). Chain structures were composed of ~ 5 oblate spheroids connected to each other at only two points each (Fig. 6d). Many spheres in these chains had concave indents on spheroid faces (Fig. 6d).

Individual oblate spheroids had an average diameter of 9.9 μm (range = 6.5–12.8 μm, $N = 51$). The oblate spheroids had crenulated edges and were composed of multiple flat hexagonal plates, which were exposed on the spheroid's top and bottom (Fig. 6a). Hexagonal plates were aligned side by side along the plate's long axis in each spheroid. The plates had the same geometry as the hexagonal plates described above (with average length = 2.8 μm and average width = 2.9 μm). In cross section across a broken face, oblate spheroids contained either isopachous lamina with radiating crystals, or alternating light- and dark-toned concentric laminations (Fig. 6f).

Smooth spheres: Smooth spheres formed masses that were in contact with each other on quartz boxwork septa in QBG rock voids (Fig. 7a). The smooth sphere masses were present throughout QBG rock voids and encompassed areas

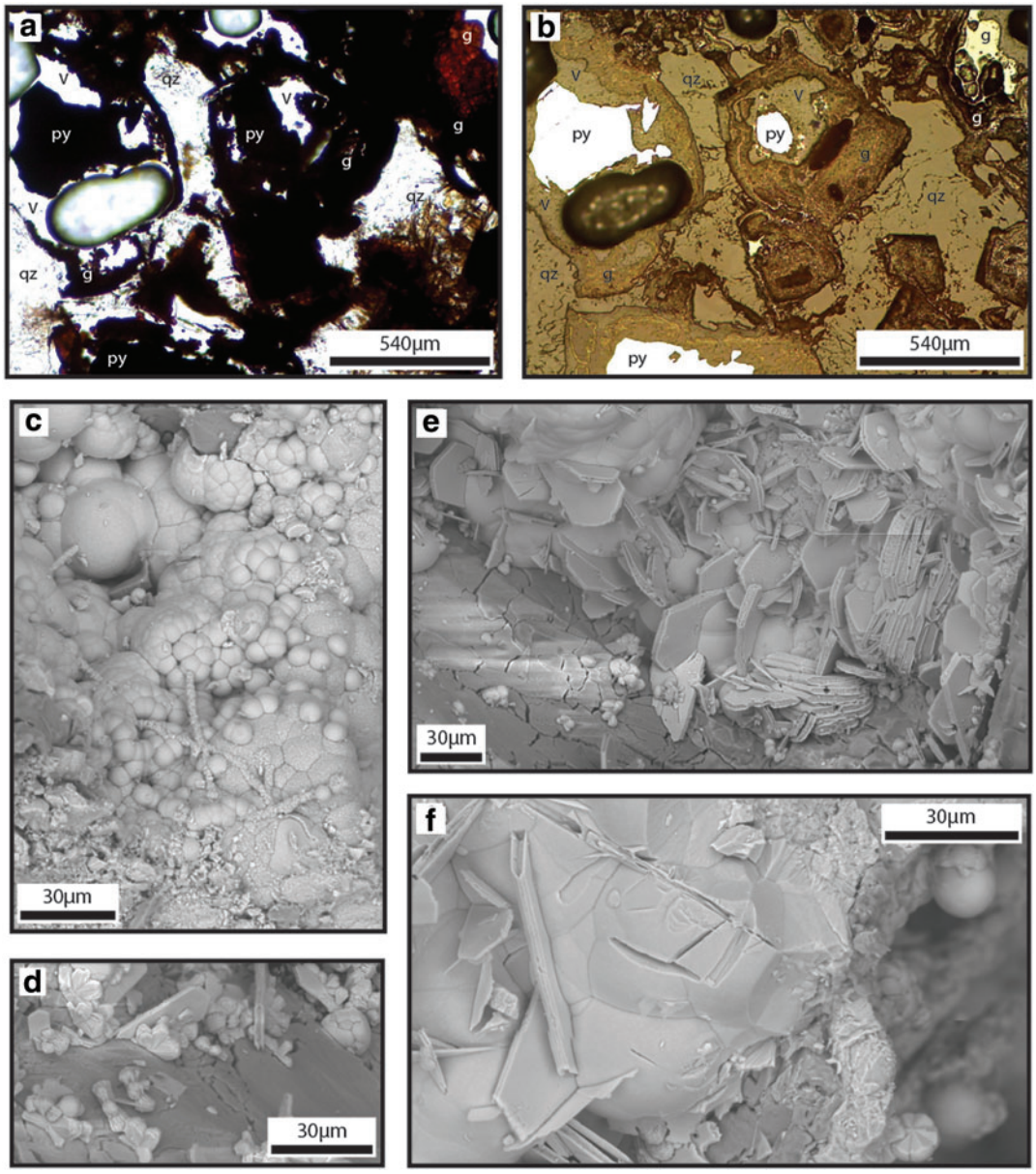

FIG. 4. Mineral textures in QBG rocks. Panel (**a**) is a transmitted light photomicrograph; panel (**b**) is the same thin section in reflected light. These panels show the interface of goethite (g) oxidizing from pyrite (py) within negative pseudomorphs defined by quartz (qz), and void space (V). Panels (c–f) are environmental scanning electron microscopy (ESEM) mosaic SE images. (**c**) Smooth spheres overlay bumpy HFO filaments and knurled surfaces. (**d**) Hexagonal plates overlay tabular crystals. (**e**) Large tabular crystals are directly attached to the surface of the quartz boxwork. (**f**) Tabular crystal interiors are exposed and reveal a recessive material with irregular surfaces and substantial pitting that was eroded back from the exposed crystal surface. Smaller smooth hemispheres overlay tabular crystals. (Color graphics available at www.liebertonline.com/ast)

of thousands of cubic micrometers. Smooth spheres were attached to either laminated HFO (hemi)spheres or a thin (<10 μm) crystalline HFO layer that directly attached to the quartz boxwork (Fig. 7e). Smooth spheres were present on top of oblate spheroids (Fig. 6a), knurled surfaces (described below), and bumpy HFO filaments (Fig. 5a, 5c, 5d). Hatched surfaces (described below; Fig. 5c) were present on top of smooth spheres. Smooth spheres either formed agglomerations or were present on top of bumpy HFO filaments but did not form long, curvilinear, self-supported structures themselves like the bumpy HFO filaments. Agglomerations were present as hundreds to thousands of smooth spheres connected to each other at several points (Fig. 7). Many spheres in the agglomerations had concave indents on spheroid faces (Fig. 7b, 7c, 7d). Hundreds of smooth spheres were present on top of bumpy HFO filaments when both were present and formed chains of spheres that vaguely outlined the original bumpy HFO filament morphology. Multiple or individual smooth spheres connected adjacent filaments.

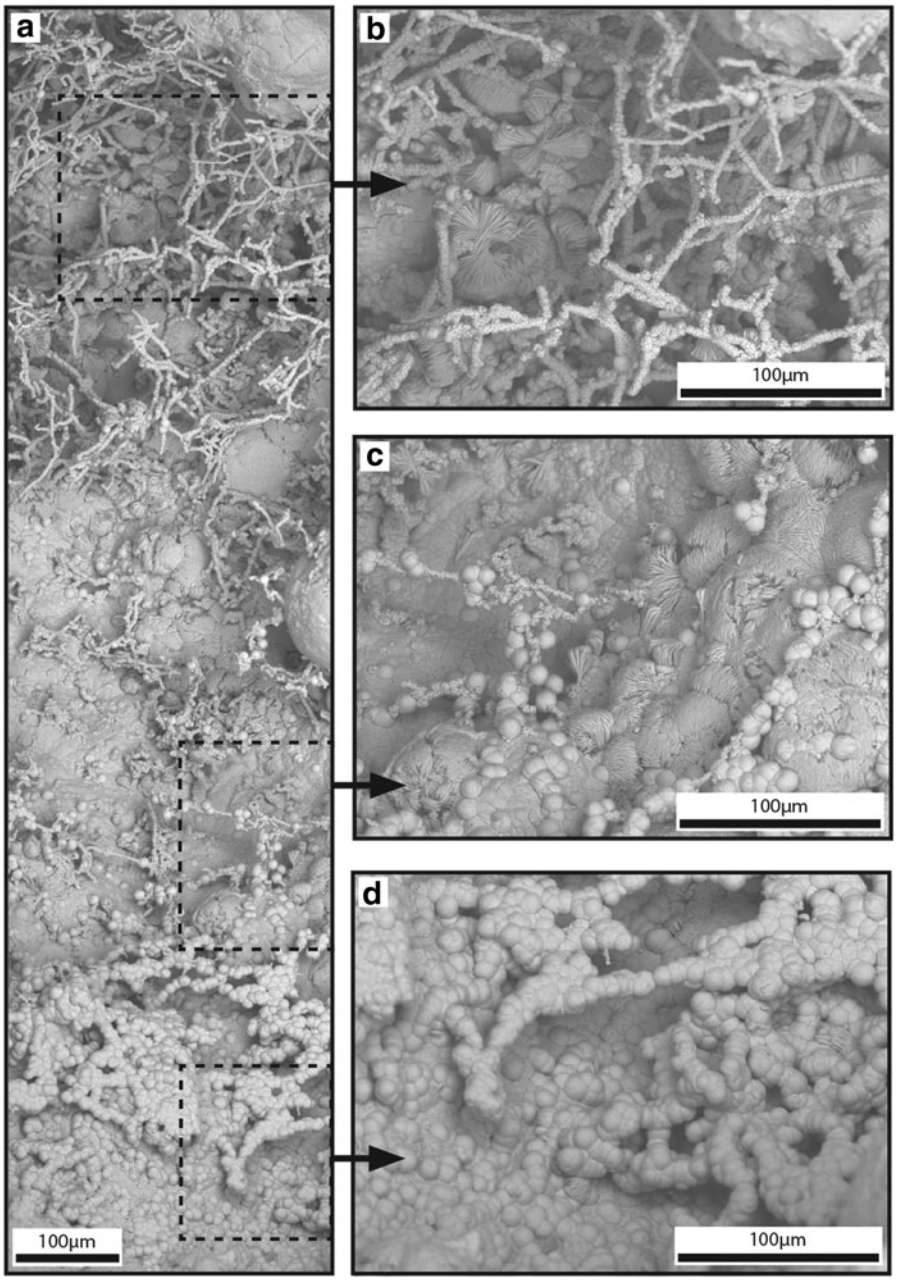

FIG. 5. Bumpy HFO filaments in QBG rocks. Panels (a–d) are SEM mosaic SE images acquired with ESEM. (**a**) Overview SEM mosaic of bumpy HFO filaments, smooth spheres, and hatched surfaces. Areas of close-up images shown for (b), (c), and (d). (**b**) Curvilinear bumpy HFO filaments form networks of overlapping filaments. (**c**) Smooth spheres on bumpy HFO filaments. Bladed crystals form hatched surfaces that overlay smooth spheres and bumpy HFO filaments. (**d**) Bumpy HFO filaments completely coated with smooth spheres.

Individual smooth spheres exhibited variable diameter. Smooth spheres on bumpy HFO filaments had an average diameter of 11.5 μm (range = 10.0–14.7 μm, $N = 24$). Smooth spheres in agglomerations had an average diameter of 12.2 μm (range = 2.9–30.5 μm, $N = 100$). In agglomerations, smaller spheres were present on the surface of larger spheres (Fig. 7b). Smaller spheres were also observed inside broken faces of larger spheres (Fig. 7c). In cross section across a broken face, smooth spheres retained either concentric lamina with radiating crystals, or alternating light- and dark-toned concentric laminations (Fig. 7d).

Bladed crystals (fans, bowties, and pinwheels): Bladed crystals formed lamellar aggregations of bladed structures that were spaced from touching to tens of micrometers apart in QBG rock voids defined by quartz boxwork septa (Fig. 8). Bladed structures were present throughout QBG rock voids, encompassing areas of thousands of cubic micrometers. The bladed structures formed fans, bowties, and pinwheels that individually ranged from $\sim$10 to 25 μm in radius. Bladed structures were composed of tens to hundreds of elongate and flattened HFO bladed crystals that radiated from a central nucleation point. Pinwheel structures were present as bladed crystals that completely surrounded (in 360°) a nucleation point (Fig. 8d). Fan structures extended out in one direction from a nucleation point and formed <30° to $\sim$90° fans (Fig. 8b). Bowtie structures were present as bladed crystals that formed a mirror image on either side of a nucleation site. Frequently, several long blades extended across the mirror axis from one side of the bowtie to the other side (Fig. 8b). All bladed crystal morphologies were

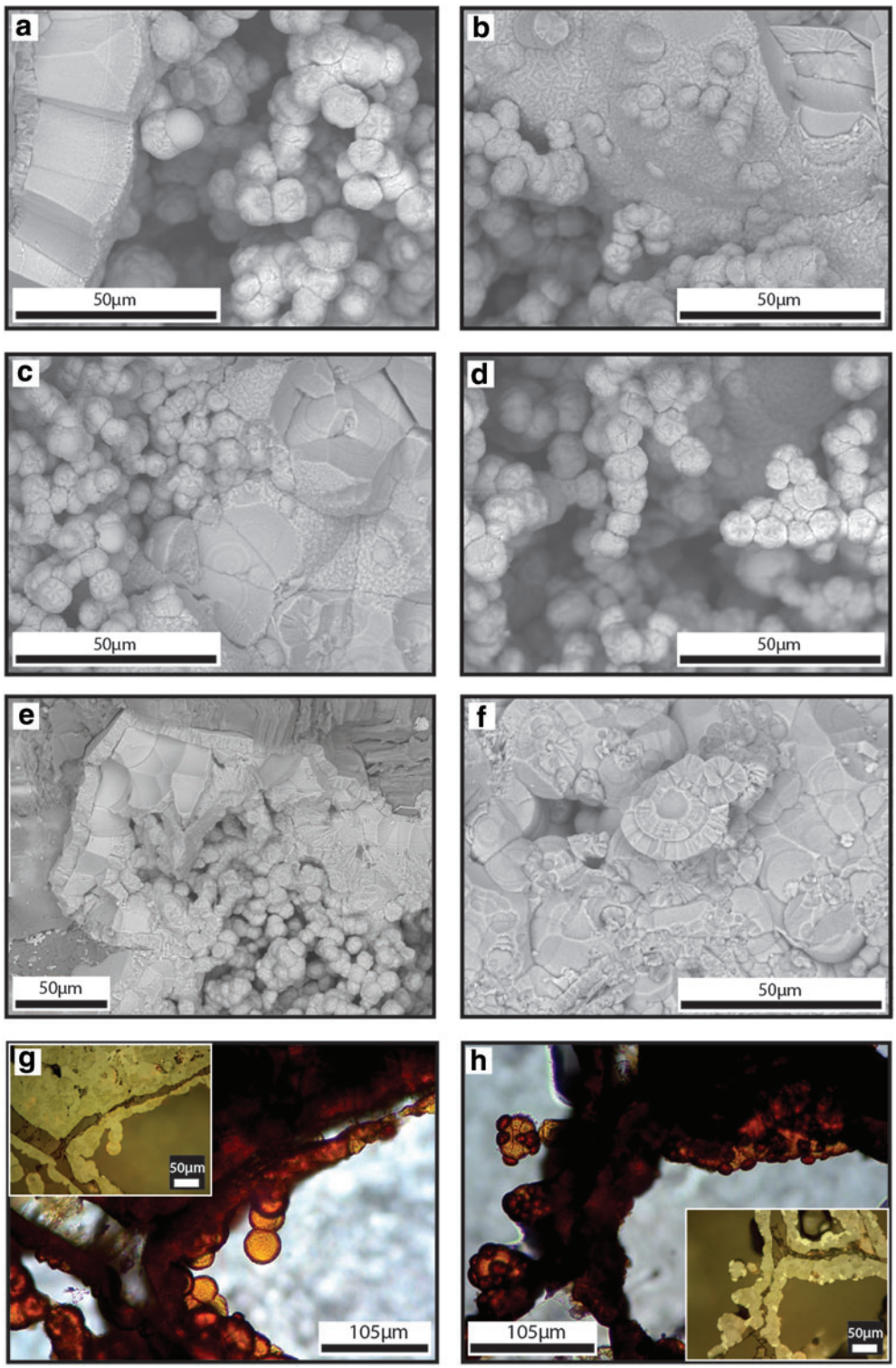

FIG. 6. Oblate spheroids in QBG rocks. Panels (a–f) are SEM mosaic SE images acquired from ESEM. Panels (g–h) are transmitted light photomicrographs; insets are reflected light photomicrographs. (**a**) Laminated HFO (hemi)spheres attached to quartz boxwork septa and oblate spheroids. (**b**) Crenulated edges from oblate spheroids are expressed as a knurled surface. (**c**) Light- and dark-toned concentric laminations are preserved within laminated HFO (hemi)spheres. (**d**) Oblate spheroids accumulated side by side but did not form curvilinear, self-supported features consistent with bumpy HFO filaments. (**e**) Oblate spheroids attached to laminated HFO (hemi)spheres form agglomerations. Some surfaces of laminated HFO (hemi)spheres demonstrate conchoidal fracturing. (**f**) In cross section, spheres retain isopachous lamina with radiating crystals and alternating light- and dark-toned concentric laminations. (**g**) Thin section example of oblate spheroids aligned side by side, as in (d). Inset shows reflected light view. (**h**) Generations of large and small (hemi)spheres are observed, with younger small hemispheres (red in transmitted light, white in reflected light inset), on older larger spheres and surfaces (yellow in transmitted light, light gray in reflected light inset). (Color graphics available at www.liebertonline.com/ast)

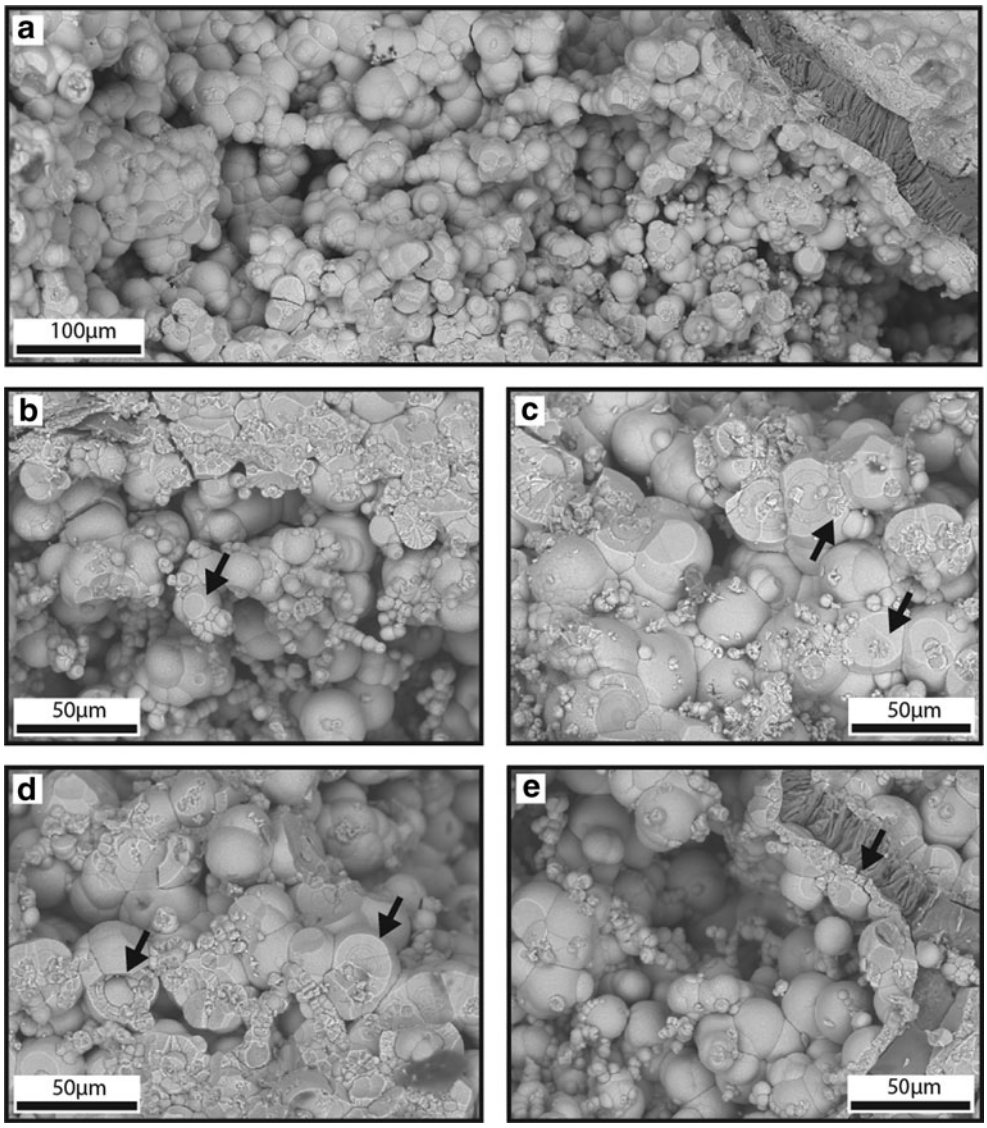

FIG. 7. Smooth spheres in QBG rocks. Panels (a–e) are SEM mosaic SE images acquired from ESEM. (**a**) Smooth spheres form agglomerations that fill voids. (**b**) Smooth spheres exhibit a great size range with larger spheres forming the textural framework and smaller spheres nucleating on larger spheres. Some spheres exhibit a concave indent on one side. (**c**) Smaller spheres on large sphere surfaces are present inside large spheres (arrow). (**d**) In cross section, spheres retain either isopachous lamina with radiating crystals (arrow), or alternating light- and dark-toned concentric laminations (arrow). (**e**) At the quartz boxwork interface, HFO forms an isopachous layer attached to the quartz (darker phase) boxwork (arrow). Botryoidal goethite hemispheres are present on the isopachous surface and on top of each other extending out into the void.

attached to other HFO structures including bumpy HFO filaments (Fig. 8d) and to each other (Fig. 8c), rather than to quartz boxwork septa. Individual bladed crystals averaged 8.8 μm wide by 21.1 μm long by 0.7 μm thick. Individual blades in a given structure were equally wide, and these defined the width of the fan, bowtie, or pinwheel structure.

Hatched surfaces: Hatched surfaces were tens of micrometers thick and extended for tens to hundreds of micrometers in length in QBG rock voids. They were composed of bladed crystals (described above; Fig. 8). Hatched surfaces overlaid both bumpy HFO filaments and smooth spheres on bumpy HFO filaments (Fig. 5c).

4.3. Remobilized iron deposits

Remobilized iron deposit (IO) samples lacked a quartz boxwork framework and were composed solely of HFO and HFO clastic material. IO rocks were generally present as locally restricted centimeter-scale coatings on QBG rocks. Some IO rocks contained botryoidal HFO that formed colloform to laminated textures in cross section, whereas other IO rocks contain laminated HFO with no botryoidal component. Although IO rocks did not contain quartz boxwork, they were typically adjacent and attached to QBG-type rocks (Fig. 2i). The HFO-dominated rocks were typically several

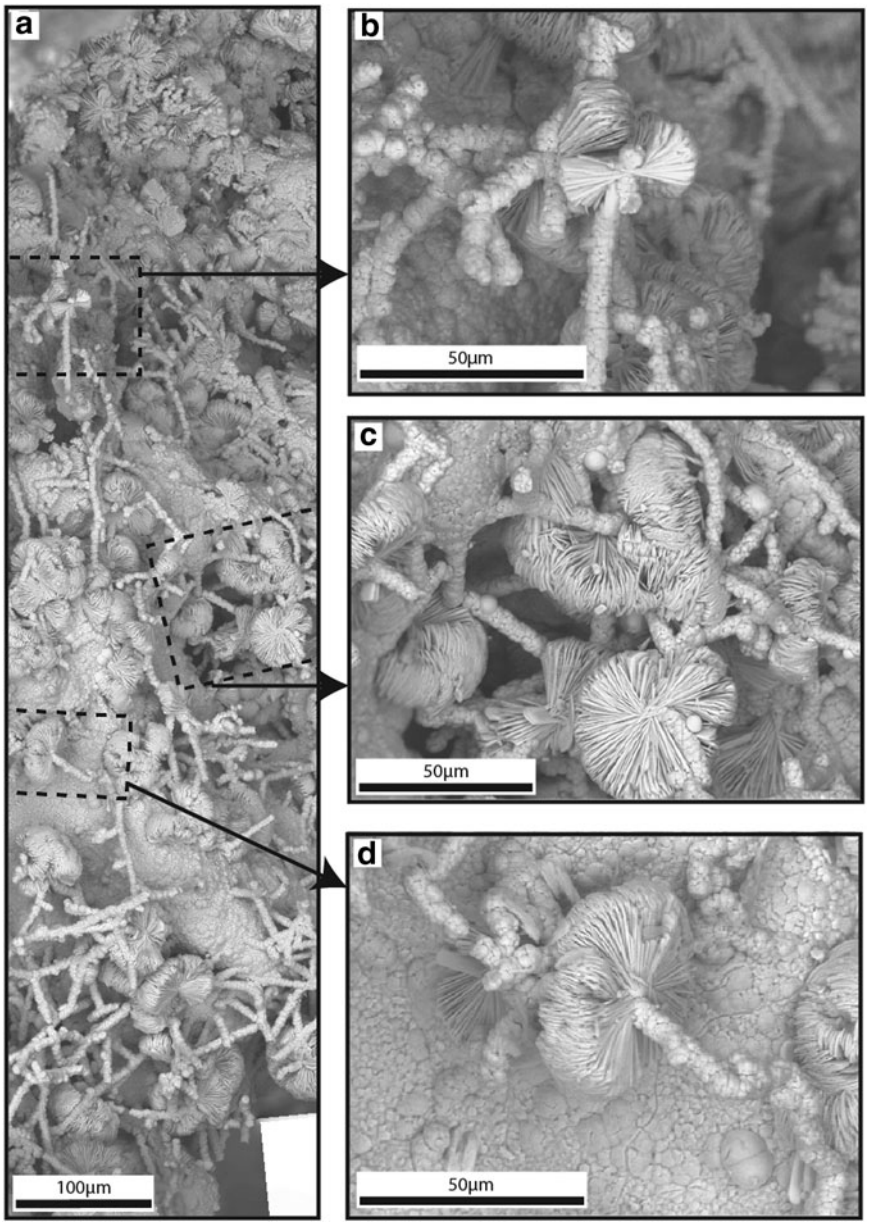

FIG. 8. Bladed crystals in QBG rocks. Panels (a–d) are SEM mosaic SE images acquired from ESEM. (**a**) Overview SEM mosaic of elongate and flattened bladed crystals that radiate from central nucleation sites and form fan, bowtie, and pinwheel structures. Dashed boxes indicate location of magnified images shown in panels (b), (c), and (d). (**b**) Fan and bowtie structures form on some bumpy HFO filaments. (**c**) Bladed crystals frequently overlay bumpy HFO filaments and form hatched surfaces. (**d**) Pinwheel structures form when bladed crystals completely surrounded (in 360°) a nucleation point.

millimeters to centimeters thick. There were six diverse hand sample–scale subtypes identified: brightly colored laminated HFO, dull laminated HFO (Supplementary Material), dendritic HFO masses, coalesced vertical columns, siliceous HFO mass, and clast- and HFO filament–bearing HFO masses. Certain subtypes of this rock contained mineralized filamentous features interpreted as filamentous microbial biosignatures, while other subtypes contained lithified clastic material and laminated and patterned HFO. The detailed descriptions (below) of these different features contributed to the identification of filamentous microbial biosignatures in the remobilized iron deposits.

4.3.1. Descriptions of hand sample–scale mineralogy and texture.

(1) *Brightly colored laminated HFO:* Brightly colored laminated HFO formed a thin coating of IO rock on the surfaces of QBG rocks (Fig. 2j). Brightly colored laminated HFO was often present adjacent to dull luster QBG. The brightly colored laminated HFO formed a patchy and irregular coating on dull luster QBG that was tens of centimeters wide, and the coating itself was >1 cm thick. Brightly colored laminated HFO was composed of tens to hundreds of thin (≤1 mm) laminae in a variety of colors (black and bright yellow, red, and orange), observable in cross section.

(2) *Dendritic HFO masses:* Dendritic HFO masses formed a thin coating of IO rock on the surfaces of QBG rocks (Fig. 2i). Dendritic HFO masses were often present adjacent to dull luster QBG and sometimes present adjacent to brightly colored laminated HFO. The dendritic HFO masses formed a patchy and irregular coating that was tens of centimeters wide and long, and the coating itself was rough, uneven,

and a few centimeters thick. Dendritic HFO masses consisted of hundreds of millimeter-scale mineral dendrites and smooth mineral sheets that covered tens to hundreds of dendrites. These HFO sheets either muted the appearance of dendrites or completely covered over them and formed a smooth surface up to several centimeters wide. Each dendrite was ≤1 mm in diameter and extended only a few centimeters from the substrate. Dendrites tapered to a thick blocky point over their short length (several millimeters) and were black or dark-colored on the surface. In cross section, dendrites contained 2–3 concentric laminae defined by orange or yellow cores and 2–3 concentric black bands.

(3) *Coalesced vertical columns:* Coalesced vertical columns formed vertically oriented, coalesced columns of IO in a covered alcove of QBG rock (Fig. 2l). Coalesced columns were light brown to yellow in color, knobby, >5 cm wide and >6 cm long, and closely spaced to each other. Individual columns were <1 to 2 mm in diameter and wider at the top of the column with tapering toward the bottom. Column interiors were a deep red color and in cross section exhibited complex lamination around multiple nuclei.

(4) *Siliceous HFO mass:* Siliceous HFO mass formed a 2.6 cm thick coating on the surface of a QBG rock (Fig. 2m). The siliceous HFO mass was 26 mm thick by >52 mm wide by 1.5–4.0 mm long. Much of the rock was a red-brown color HFO. The red-brown HFO material surrounded white silica-rich deposits and quartz grains.

(5) *Clast- and HFO filament–bearing HFO masses:* Clast- and HFO filament–bearing HFO masses formed a deposit of IO rock that was up to tens of centimeters in diameter on the surfaces of QBG rocks (Fig. 2n). This deposit was composed of a variety of textures and materials, including laminated HFO masses (described below); lenses of oriented, smooth HFO filaments (described below); and lithified weathered quartz and HFO grains in an iron-rich matrix. Regions with weathered quartz and HFO grains were present in areas up to several centimeters wide and thick and 1–2 cm tall. Clast sizes ranged from fine sand to granule-sized and were composed of weathered white quartz and yellow-to-orange-colored HFO particles in a dark red-to-orange HFO matrix. Oriented, smooth HFO filaments formed lenses several centimeters wide and tall and ≤1 cm thick. Lenses of smooth HFO filaments were dark red to brown in color and formed areas of high porosity.

4.3.2. Descriptions of microscale mineral morphology. At the micrometer scale, IO rocks contained a variety of mineral textures including lenses of oriented and smooth HFO filaments, patterned HFO masses, and laminated HFO masses.

Smooth HFO filaments: Hundreds to thousands of smooth HFO filaments formed a networklike structure of overlapping filaments that ranged from touching to spaced tens to hundreds of micrometers apart (Fig. 9). Smooth HFO filaments were present in restricted regions of IO rocks, formed weakly to strongly oriented fabrics (Fig. 9b, 9c, 9f), and covered areas of >2.8 mm by >0.4 mm. Filaments commonly extended into void space unsupported on one end of the filament (Fig. 10c, 10d). The smooth filaments were connected to HFO-bearing substrates, such as laminated HFO masses (described below) and clast-bearing HFO masses. Smooth HFO filaments intersected at angles ranging from subparallel to perpendicular. Individual filaments were composed of wedge-shaped HFO crystals with average 1.1 μm width that formed a smooth to colloform surface expression (Fig. 9d, 9e) on the exterior of the filament. Filaments averaged 7.8 μm in diameter (range = 1.1–19.7 μm, N = 127 filaments) and averaged 97.0 μm in length (range = 5.8–445.9 μm), although some filaments were likely longer as not all the filament ends were exposed. Individual filaments were curvilinear to linear and cylindrical, did not branch, and had generally uniform diameter. Some smooth HFO filaments contained central lumina (average 0.5 μm in diameter, range = 0.2–1.0 μm, N = 6). The HFO mineral morphologies that frequently radiated from the central lumen were colloform to acicular. However, some lumina were surrounded by an irregular crystalline to granular HFO texture that separated the colloform morphologies from the lumina.

Patterned HFO masses: Patterned HFO masses formed physically small regions within IO rocks (Fig. 9g). Patterned HFO masses occupied areas greater than 2.1 mm by 1.0 mm and were present adjacent to regions containing smooth HFO filaments. They were composed of naturally broken HFO surfaces. The ''pattern'' was composed of concentric laminations around circular to cylindrical nuclei in a variety of diameters and flat to curved layers of laminated HFO composed of acicular crystals. Together, these two textures formed a ''patterned'' HFO mass. The intersection between the smooth HFO filaments and the patterned HFO masses was gradational. HFO filaments crossed the boundary into the patterned HFO mass area. At that intersection, the acicular crystals and concentric laminations in the patterned HFO mass were observed as extensions of the HFO filaments. Concentric laminations in the patterned HFO mass ranged from 14.9 to 33.1 μm in diameter.

Laminated HFO masses: Laminated HFO masses formed physically small regions within IO rocks (Fig. 9a). Laminated HFO masses occupied areas greater than 4.0 mm wide by 5.0 mm long by 1.0 mm thick, were an iridescent dark red color in optical microscopy, and were present adjacent to patterned HFO masses. Laminated HFO masses did not contain internal patterns consistent with HFO filaments or encapsulated filaments. The boundary between patterned HFO masses and laminated HFO masses was sharp. Laminated HFO masses were composed of hundreds of naturally broken HFO laminae. Individual HFO laminae ranged from 0.7 to >5.9 μm thick and hundreds of micrometers up to ~1.0 mm in length. Individual laminae were smooth on their faces with very little microtopography in cross section. Each lamina formed an undulate isopachous coating on the underlying laminae.

4.4. Organic features

Organic features (Fig. 11) were found on PQB-type rocks. IO-type rocks contained these surficially and internally.

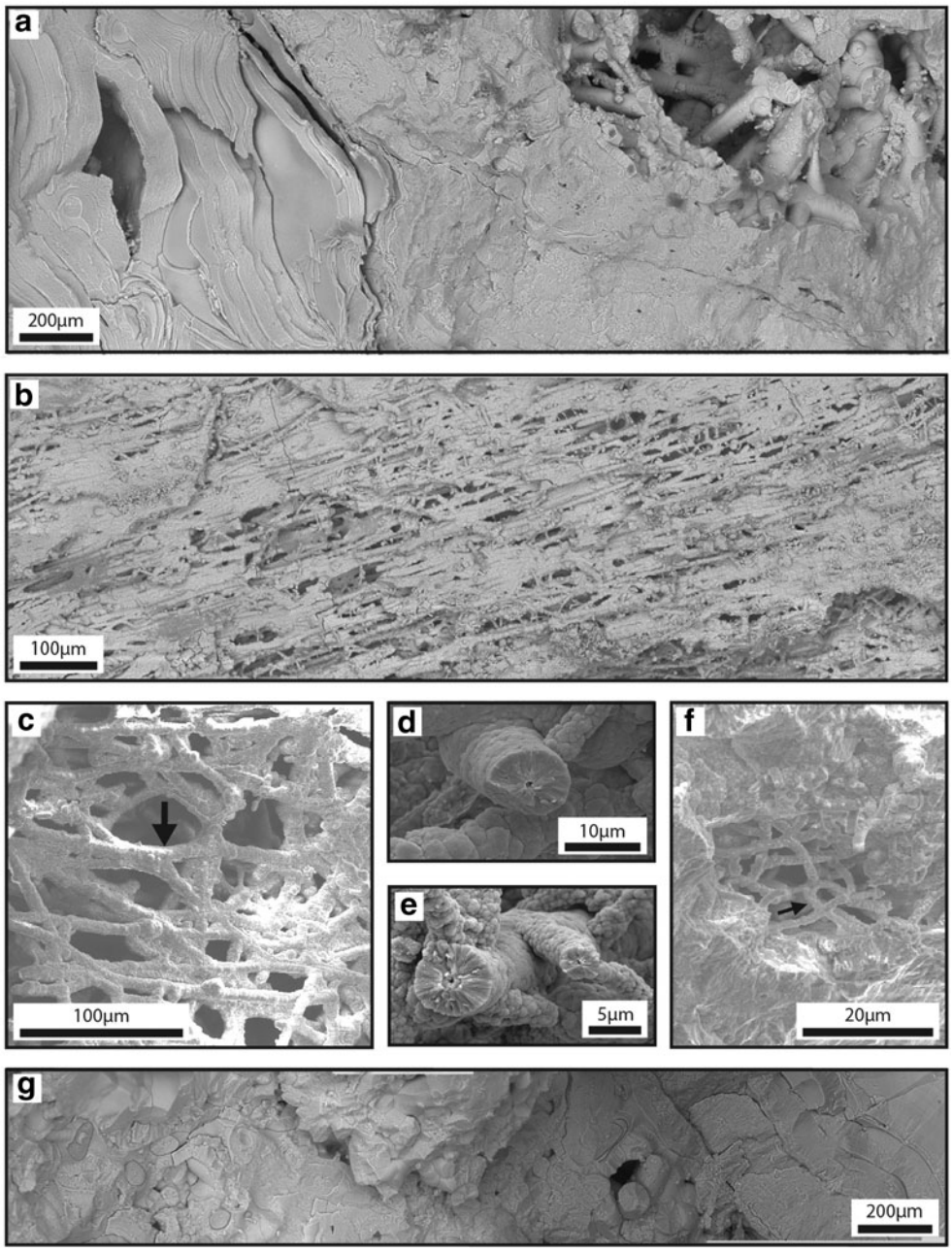

FIG. 9. Textural variation in IO rocks. All panels (a–g) are composed of SE images. Panels (a), (b), and (g) were acquired with ESEM. Panels (c–f) were acquired with FEG-SEM. (**a**) SEM mosaic of the transition from laminated HFO masses to patterned HFO masses to smooth HFO filaments (respectively from left to right). (**b**) SEM mosaic of smooth HFO filaments that form a strongly oriented linear fabric. (**c**) Smooth HFO filaments that form a more gently oriented fabric. Commonly, where HFO filaments join (arrow), filament diameter roughly equals the sum of the joined individual filaments. (**d**) Cross section of a smooth HFO filament with smooth to gently colloform exterior texture composed of wedge-shaped crystals. A lumen is preserved in the filament center. (**e**) Smooth HFO filaments with a strongly colloform exterior texture composed of wedge-shaped crystals. Central lumina are preserved. (**f**) Sinuous smooth HFO filaments with high degrees of bending, including U-loop formation (arrow). (**g**) SEM mosaic of patterned HFO masses. Putative relic filaments are outlined in thin black lines. Central cores are preserved in several examples.

Organic features were absent in QBG-type rocks. Organic features were characterized as generally surficial features with minimal to no mineralization, and they exhibited carbon peaks in EDS analysis. These features included coupled oblong spheroids, filamentous plexi, mats of organic filaments, and bundled filament networks.

4.4.1. Pyrite and quartz boxwork rock and HFO-dominated rock. *Coupled oblong spheroids:* Coupled oblong spheroids were rarely present on PQB and IO surfaces and in rock crevices (Fig. 11c). On average, these measured 36 μm long by 24 μm wide and exhibited a large C peak ($\sim$77 wt %) in EDS spectra. The two oblong spheroids were

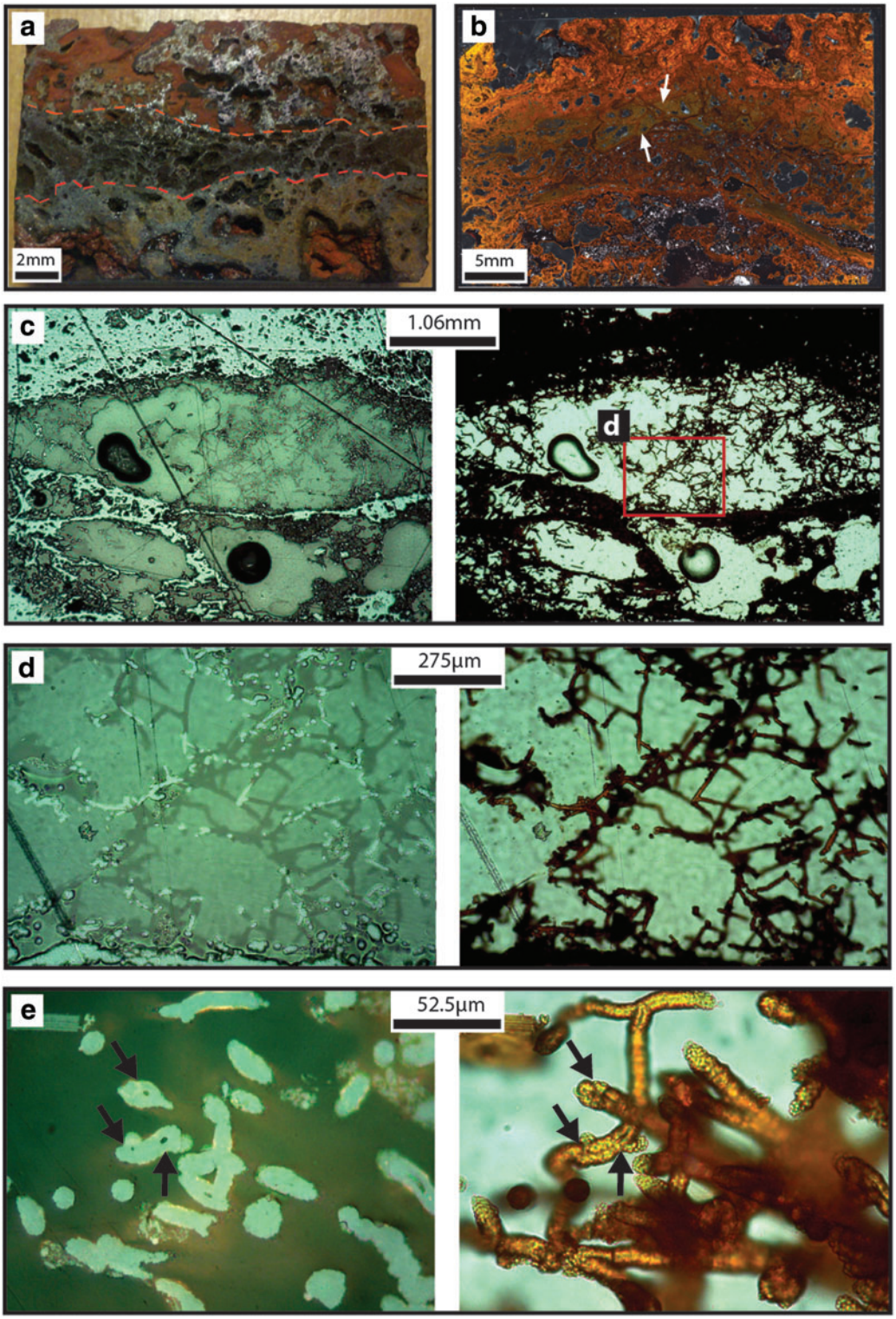

FIG. 10. Hydrous ferric oxide filaments in IO rocks. (**a**) Image of an IO rock that contains smooth HFO filaments. Dashed orange lines outline the extent of smooth HFO filaments. (**b**) Thin section photomicrograph of the IO rock from (a). HFO filaments are present in the polygonal regions filled with dark yellow HFO (arrows). Laminated and botryoidal HFO is present as bands of orange and red in the top of the image. Panels (c), (d), and (e) are a series of progressively increasing magnifications of similar structures. The left side contains reflected light photomicrographs; the right side contains the complementary transmitted light photomicrograph. (**c**) Sinuous filaments in voids form networks of overlapping filaments and gently to strongly oriented fabrics. (**d**) Magnification of panel C demonstrates the overlapping nature of filaments in three dimensions. (**e**) Magnification of region similar to panel (d) demonstrates the sinuous nature of the smooth HFO filaments. Central lumina are apparent in reflected light photomicrographs (arrows), and corresponding lumina positions at filament ends and along filament length are noted in the transmitted light image (arrows). (Color graphics available at www.liebertonline.com/ast)

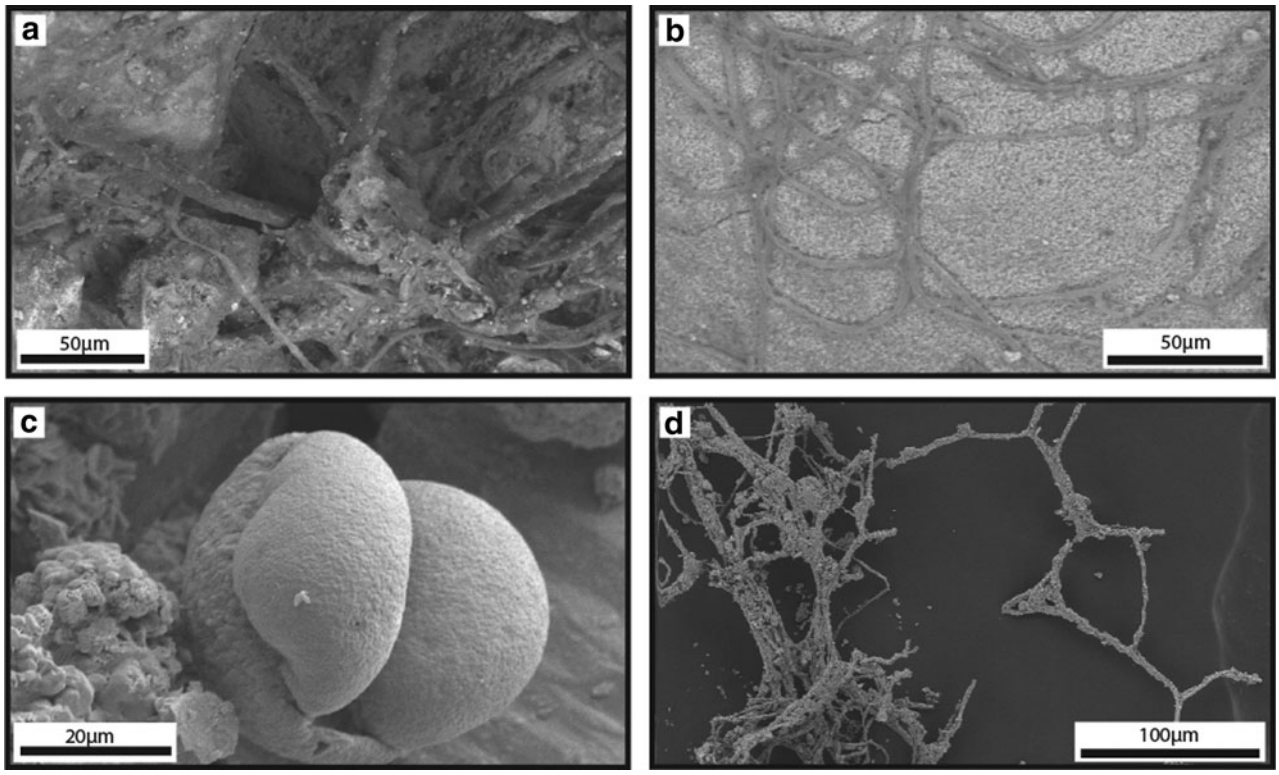

FIG. 11. Biological structures in gossan rocks. Panels (a), (c), and (d) were acquired with FEG-SEM. Panel (b) was acquired with ESEM. (**a**) BSE image of curvilinear filamentous plexi with bare tapering filaments on IO-type rocks. (**b**) SE image of mats of organic curvilinear filaments with bare, uniform-diameter filaments form overlapping filament networks, including U-loop structures, on IO-type rocks. (**c**) SE image of oblate spheroids interpreted as pollen grains are found on both PQB- and IO-type rocks. (**d**) BSE images of curvilinear bundled filament networks are made of bundled mineralized filaments and found inside regions of siliceous HFO mass.

connected at their outer edges by a granular cap (tens of micrometers in diameter). Some of these coupled oblong spheroids were free of mineral detritus, although small (approximately several micrometers wide) zones of minerals were observed on some surfaces.

4.4.2. Hydrous ferric oxide-dominated rock. *Filamentous plexi:* Filamentous plexi were rarely present on IO surfaces (Fig. 11a). The filaments that composed the plexus extended out from a central locus and formed structures greater than 0.25 mm^2 and exhibited a C peak ($\sim$14 wt %) in EDS spectra. Each plexus was composed of tens of filaments. Individual filaments averaged 6.1 μm in diameter (range = 1.7–10.1 μm, $N = 5$ filaments) and ranged from 101.2 to 239.6 μm long, although some filaments may have been longer as not all the filament ends were exposed. Individual filaments were curvilinear, did not branch, and were thicker near the central plexus and tapered toward the filament ends. Filaments were mostly bare, with little mineral coating on some filaments.

Mats of organic filaments: Mats of organic filaments formed a networklike structure of overlapping filaments in one region of an IO surface (Fig. 11b). The networklike structure was greater than 0.5 mm long by 0.4 mm wide and exhibited a C peak ($\sim$15 wt %) in EDS spectra. The network was composed of tens of filaments. Individual filaments averaged 2.0 μm in diameter (range = 1.3–2.9 μm, $N = 15$ filaments) and ranged from 57.8 to 300.2 μm long, although some filaments are likely longer as not all the filament ends were exposed. Individual filaments were curvilinear, did not branch, and had generally uniform diameters. All mats of organic filament were attached to the IO substrate along the total length of the filament and were mostly bare, with very sparse mineral coating on some filaments. Several filaments formed distinctive U-loop structures (Fig. 11b).

Bundled filament networks: Bundled filaments formed a networklike structure of overlapping filaments (Fig. 11d) inside one region of the siliceous HFO mass sample (Fig. 2m). The densely spaced networklike structure was greater than 2.5 cm tall by 3.3 cm wide and exhibited a large C peak ($\sim$43 wt %) in EDS spectra. Coupled oblate spheroids were frequently found in association with bundled filaments. The network was composed of hundreds of bundled filaments. Bundled filaments averaged 4.8 μm in diameter (range = 1.7–9.0 μm, $N = 51$ filaments), were hundreds of micrometers in length and moderately mineralized, and exhibited branching. Individual filaments within each bundle averaged 1.7 μm in diameter (range = 1.5–1.9 μm, $N = 2$ filaments) and hundreds of micrometers in length, although some filaments may have been longer as filament ends were not exposed. Individual filaments were curvilinear and a red-orange color in transmitted light under the optical microscope. They generally had uniform diameters. It was difficult to distinguish individual filaments within the bundle; therefore, it was difficult to determine whether individual filaments branched (either true or false

branching) or filaments within a bundle diverged to form apparent branches.

4.5. Filament morphology

Microbial filaments, mineral filaments, and abiotic mineral fibers were characterized by diameter, tortuosity, bending, and number of direction changes per 20 μm, similar to the approach of Hofmann *et al.* (2008). These parameters were measured on microbial filament samples (20 filaments), abiotic mineral fiber samples (10 fibers), bumpy HFO filaments from QBG samples (191 filaments), smooth HFO filaments from IO samples (127 filaments), cryptic filament samples (12 filaments), and central lumina from smooth HFO filaments (6 filament lumina), as well as microbial filaments from acidophilic and neutrophilic environments from the literature. Average, minimum, and maximum values for these parameters are reported in Table 4.

Microbial filaments from the literature that were incorporated in this study include the following: (1) Unidentified eukaryotic filaments found in the Iron Mountain mine (Richmond adit) (Schrenk *et al.*, 1998; Edwards *et al.*, 1999). (2) *Acidithiobacillus ferrooxidans*, an acidophilic Fe-oxidizer prevalent at Iron Mountain, forming filaments under PO_4 starvation conditions (Seeger and Jerez, 1993). (3) *Leptothrix*-like bacteria cultured from Río Tinto, Spain (Preston *et al.*, 2011), as well as (4) *Leptothrix* sp. microbial mats (Schieber and Glamoclija, 2007; Florea *et al.*, 2011). *Leptothrix* sp. is an iron-oxidizing bacteria found in neutrophilic environments down to $\sim$pH 6 (the higher range of pH explored in this study at Iron Mountain). (5) *Comamonas denitrificans*, a filamentous nitrate-reducing bacteria found in the gossan at Iron Mountain (Williams, 2014b).

The assessment of pairwise distinctness targeting elongate features suggested whether microbial filaments are morphologically more distinct from smooth HFO filaments, bumpy HFO filaments, cryptic filaments, and mineral fibers than these HFO filament and fiber types are from each other. The diameter, bending, and number of direction changes were compared among five elongate feature populations, one of biogenic (microbial) filaments, one of abiogenic (mineral) fibers, and three unknown (smooth HFO, bumpy HFO, and cryptic) filaments.

With a given morphological parameter, the improbability of pairwise distinctness for each biogenic-abiogenic pair is consistently lower than for abiogenic pairs (Table 5). These results indicate that biogenic filaments differ systematically from abiogenic filaments and fibers, even though the complexity of environmental conditions may preclude typical (*e.g.*, 95%) statistical confidence. Specifically, in the ''bending'' parameter, microbial filaments consistently yield an improbability of distinctness equivalent to <60% with smooth HFO filaments, bumpy HFO filaments, cryptic filaments, and mineral fibers, suggesting microbial filaments

Table 4. Measured Morphology Parameters of Gossan Features

		Diameter (μm)			*Tortuosity*			*Bending (degree/20 μm)*			*Number of direction changes/20 μm*		
	N =	*avg*	*min*	*max*	*avg*	*min*	*max*	*avg*	*min*	*max*	*avg*	*min*	*max*
HFO filaments													
All	318	8.9	1.1	32	1.1	1.0	5.0	58.5	0.5	1287	1.4	0.0	32
Bumpy	191	9.8	2.4	32	1.1	1.0	5.0	37.9	0.5	286.0	0.7	0.0	6.3
Smooth	127	7.8	1.1	20	1.1	1.0	3.2	85.9	0.6	1287	2.2	0.0	32
Smooth filament lumina	6	0.5	0.2	1.0	na	na	na	na	na	na	na	na	na
Microbial filaments													
FP	5	6.1	4.4	6.9	1.1	1.0	1.3	41.7	14	59.10	1.4	0.6	2.0
MOF	15	2.0	1.3	2.9	1.5	1.0	1.9	22.6	5.7	54.40	0.9	0.4	1.6
Literature microbial filaments													
IMM eukaryotes (Edwards *et al.*, 1999)	1	1.6	na	na	1.9	na	na	97.6	na	na	2.0	na	na
IMM eukaryotes (Schrenk *et al.*, 1998)	2	1.5	1.4	1.6	1.0	1.0	1.0	129	92.3	166	6.3	4.3	8.4
Acidithiobacillus ferrooxidans (Seeger and Jerez, 1993)	6	0.4	0.4	0.5	1.0	1.0	1.0	372	41.5	892	1.8	0.0	5.9
Leptothrix-like bacteria, Río Tinto, Spain (Preston *et al.*, 2011)	7	0.8	0.7	1.0	1.0	1.0	1.0	82.6	24.3	174	3.0	0.0	5.9
Leptothrix sp. (Florea *et al.*, 2011)	1	1.2	na	na	1.0	na	na	145	na	na	2.9	na	na
Leptothrix sp. (Schieber and Glamoclija, 2007)	3	2.2	1.9	2.5	1.0	1.0	1.0	26.3	15.8	46.1	0.0	0.0	0.0
Comamonas denitrificans (Gumaelius *et al.*, 2001)	2	0.8	0.8	0.8	1.7	1.1	2.3	356	227	485	6.8	3.37	10.3
Mineral fibers	10	1.7	0.6	6.9	1.0	1.0	1.0	15.9	0.0	77.60	0.5	0.0	2.9
Cryptic filaments	12	0.5	0.2	0.7	1.2	1.0	1.9	126	47	271.9	0.9	0.0	4.1
Oblate spheroids	51	9.9	6.5	13	na	na	na	na	na	na	na	na	na
Smooth spheres													
In agglomerations	100	12	2.9	31	na	na	na	na	na	na	na	na	na
On bumpy HFO filaments	24	12	10	15	na	na	na	na	na	na	na	na	na

FP = filamentous plexi; IMM = Iron Mountain mine/Richmond adit; MOF = mats of organic filaments; na = not applicable.

TABLE 5. IMPROBABILITY OF PAIRWISE DISTINCTNESS

DIAMETER	*Biogenic*—microbial filament	*Putative biosignature*—smooth HFO filament	*Putative biosignature*—bumpy HFO filament	*Abiogenic*—mineral filament	*Unknown*—cryptic filament
Biogenic—microbial filament	X	0.11	0.27	0.92	0.53
Putative biosignature—smooth HFO filament		X	0.80	0.08	0.03
Putative biosignature—bumpy HFO filament			X	0.25	0.19
Abiogenic—mineral filament				X	na
Unknown—cryptic filament					X
BENDING	*Biogenic*—microbial filament	*Putative biosignature*—smooth HFO filament	*Putative biosignature*—bumpy HFO filament	*Abiogenic*—mineral filament	*Unknown*—cryptic filament
Biogenic—microbial filament	X	0.59	0.52	0.49	0.65
Putative biosignature—smooth HFO filament		X	0.79	0.67	0.77
Putative biosignature—bumpy HFO filament			X	0.68	0.30
Abiogenic—mineral filament				X	na
Unknown—cryptic filament					X
NUMBER OF DIRECTION CHANGES	*Biogenic*—microbial filament	*Putative biosignature*—smooth HFO filament	*Putative biosignature*—bumpy HFO filament	*Abiogenic*—mineral filament	*Unknown*—cryptic filament
Biogenic—microbial filament	X	0.65	0.49	0.45	0.59
Putative biosignature—smooth HFO filament		X	0.70	0.60	0.51
Putative biosignature—bumpy HFO filament			X	0.74	0.48
Abiogenic—mineral filament				X	na
Unknown—cryptic filament					X

Comparison between diameter, bending, and number of direction changes for microbial filaments, smooth and bumpy HFO filaments, mineral fibers, and cryptic filaments. Pairs with >60% probability are shaded dark gray. Only microbial filaments are biogenic in origin. Other categories are neither microbial nor inherently biogenic, which we consequently label ''putative biosignature,'' ''abiogenic,'' or ''unknown.''

are systematically different. Pairs of HFO filaments, cryptic filaments, and mineral fibers yield consistently higher probabilities (>60%) with each other (Table 5). This is consistent with the statistical distinctness of biogenic filaments from the other elongate features. The other elongate features, including mineral fibers, bumpy and smooth HFO filaments, and cryptic filaments, are effectively statistically indistinguishable from each other.

5. Discussion

The diversity of rock types and microscale iron mineral morphologies identified in the gossan suggest that pyrite oxidation substantially mobilizes iron. This remobilized iron can precipitate onto any available substrate, including microbial filaments, to form HFO mineral filaments. Preserved HFO filaments satisfy specific criteria used to identify biosignatures in rocks, and their context provides insights into formation mechanisms. Two conceptual schematics are presented here to elucidate the formation and preservation of HFO filaments in the gossan, including how microscale physical and geochemical environments affect HFO filament formation.

5.1. Iron mineral precipitation

Iron mineral precipitation is a direct result of the (mostly biotic but some abiotic) oxidation of iron and sulfur in pyrite at Iron Mountain. Fluids that interact with oxidizing pyrite acquire $Fe(II)_{(aq)}$, which is continually oxidized by Fe(II)-oxidizing microbes (such as *Acidithiobacillus ferrooxidans* and *Leptospirillum* sp.) and abiotic geochemical reactions. As Fe(III) is produced, primarily by the microbial oxidation of iron, the solution reaches saturation with HFO or iron-sulfate salts (Nordstrom and Alpers, 1999b; Alpers *et al.*, 2003). Iron-sulfate salts that precipitated, such as copiapite group minerals (white tabular crystals, Supplementary Material), halotrichite group minerals (fibrous efflorescent crystals, described above), and jarosite group minerals require very specific pH, redox, temperature, and relative humidity conditions. For example, copiapite group minerals are known to precipitate at Iron Mountain from fluids with $pH = -0.9$ (Jamieson *et al.*, 2005), and ferricopiapite was estimated to be stable in the pH range 0–1 (Majzlan *et al.*, 2006). In the Iron Mountain gossan, mixed-valence copiapite group mineral salts precipitated first, followed by mixed-valence halotrichite group salts. Jarosite group minerals form at pH <3 and precipitated on rhyolite instead of in contact with pyrite. The timing and spatial distributions of these minerals suggest that the salts precipitated during ongoing fluid oxidation, with iron dominated first by Fe(II), then mixed valence [Fe(II), Fe(III)], and finally Fe(III) (Alpers *et al.*, 2003). The distribution of salt minerals in the gossan at Iron Mountain is similar to that within the Richmond Mine at Iron Mountain (Alpers *et al.*, 2003),

suggesting that the processes controlling salt formation are similar in the two environments, although the mine effluent is more acidic and the mine environment produces a much higher relative humidity conducive to salt formation.

The presence of highly soluble salts in gossan requires that no fresh water flowed over them. Rainfall is common in the winter at Iron Mountain (Alpers *et al.*, 2003), so these salts must either have formed since the last significant rainfall or they were protected from rain. Iron-sulfate salts were observed in shallow alcoves in rock faces, which were likely to be wetted by rain with even a small amount of wind. Thus, it is likely that at least some of these salts precipitated within a season or at most a few years before samples were collected. Consequently, their presence demonstrates that fluids in the gossan are still transporting iron and sulfur and precipitating salts during dry intervals.

Volumetrically, HFO is much more abundant than iron-sulfate salts. HFO precipitated on many different surfaces, ranging from inside pyrite pseudomorphs to exposed surfaces and debris such as pollen grains (coupled oblong spheroids, Supplementary Material). HFO coatings on QBG rocks as well as textures in IO rocks require precipitation of HFO near, or on, the surface. QBG rocks often have HFO surface coatings, and IO-type rocks often formed on exposed surfaces of QBG-type rocks. In IO rocks, dendritic HFO masses, coalesced vertical columns, and clast- and HFO-filament-bearing masses all have textures that require mineral precipitation in either large voids or on exposed surfaces. For example, brightly colored laminated HFO and dendritic masses have textures that show accretion away from a surface, which requires flow of iron-bearing fluids across those surfaces. In contrast, fluids also percolated through soil and cracks in rock, producing textures like coalesced vertical columns of HFO when they encountered caverns or alcoves. Many of the textural variations in IO-type rocks come from the geometry and location of surfaces, style of fluid flow, influx of detrital grains, and biological contributions such as microbial mat growth.

Hydrous ferric oxide precipitation is likely ongoing. The presence of pollen grains with HFO coatings demonstrates that at least some HFO precipitation occurred after exposure of the host rocks and the growth of pine trees. Pine pollen grains could have fallen onto rock surfaces and been coated by HFO, which would require precipitation of the HFO from water flowing over the ground surface. Alternatively, pollen could have filtered into open cracks and then been coated by HFO in the subsurface. Either example demonstrates that HFO precipitated in the current environment. In addition, the presence of HFO filaments is consistent with HFO precipitation on microbial filaments, some of which are still present in samples.

5.2. Conceptual schematic for HFO filament formation

Recent and modern iron mobility in the gossan provides the mechanism for the formation of HFO filaments. The texture of HFO filaments and their overall geometry depend on fluid flow, mineralization processes, and the geometry of the surface on which HFO minerals nucleate. HFO commonly nucleated on preexisting filaments. The origin (or origins) of these filaments is evaluated within the context of biosignature identification in a later section. Here, we evaluate the effects of fluid flow and mineralization processes on HFO filament formation in voids in *in situ* gossan and as a component of surface coatings in remobilized iron deposits.

5.2.1. Bumpy HFO filament formation in *in situ* gossan. By using the geometry and textures in bumpy HFO filaments from *in situ* gossan, the sequence of HFO precipitation events can be reconstructed. Initial mineral precipitation, either passive or active (by the metabolism of iron-oxidizing organisms), occurred on preexisting filaments. Bare microbial filaments are present in the *in situ* gossan (Fig. 12a) and may have formed the initial nucleation surfaces. Initial HFO precipitation consisted of submicrometer particles as observed on microbial filaments with only partial coatings. As submicrometer HFO particles nucleated and coalesced, they created thicker coatings on the filaments, which eventually became the preserved bumpy HFO filaments (Fig. 12b). The next stages of mineralization varied from place to place. In some places, mineralization stopped, but in others, smooth spheres nucleated on the bumpy HFO filaments (Fig. 12c). In some cases, knurled and hatched surfaces coated bumpy HFO filaments, reduced void space, and encapsulated some HFO filaments.

The observed diversity in HFO mineral morphologies (Figs. 4–9) suggests spatial variations in water geochemistry and flow. The quartz boxwork in *in situ* gossan limited permeability, and the variable percolation and chemistry of waters at, or close to, saturation with Fe(III) likely led to precipitation of HFO with a variety of textures. The thickness of coatings varied significantly from sample to sample (Fig. 13), likely reflecting the duration and volume of mineralizing fluid flowing through specific voids. Low flow rates likely led to slow mineral precipitation. Slow precipitation rates are consistent with the observed mineralogy and allowed formation of distinct mineral morphologies, such as smooth spheres, oblate spheroids, bladed crystals, and the other euhedral mineral morphologies.

5.2.2. Smooth HFO filament formation in remobilized iron deposits. The physical flow characteristics that led to accumulation of HFO in the remobilized iron deposits were different than those within the quartz boxwork. The remobilized iron deposits formed on rock surfaces where flow was not limited by permeability, creating a different suite of rock textures.

Hydrous ferric oxide filaments in remobilized iron deposits also nucleated on preexisting filamentous structures, likely bare microbial filaments (Fig. 14b). Mats of these filaments coated lithified clastic material composed of weathered quartz and HFO grains (Fig. 14a). The sand-to-granule-sized clasts require rapid water flow to be transported. Rapid water flow is also suggested by the strongly oriented linear fabric of the filaments, as is commonly observed in streamer fabrics in spring deposits (Walter *et al.*, 1996, 1998; Hofmann and Farmer, 2000). In the gossan, oriented filaments were lithified with initial minerals consisting of wedge-shaped HFO crystals (Fig. 14c). The wedge-shape crystal morphology may have formed due to competitive growth, with fewer

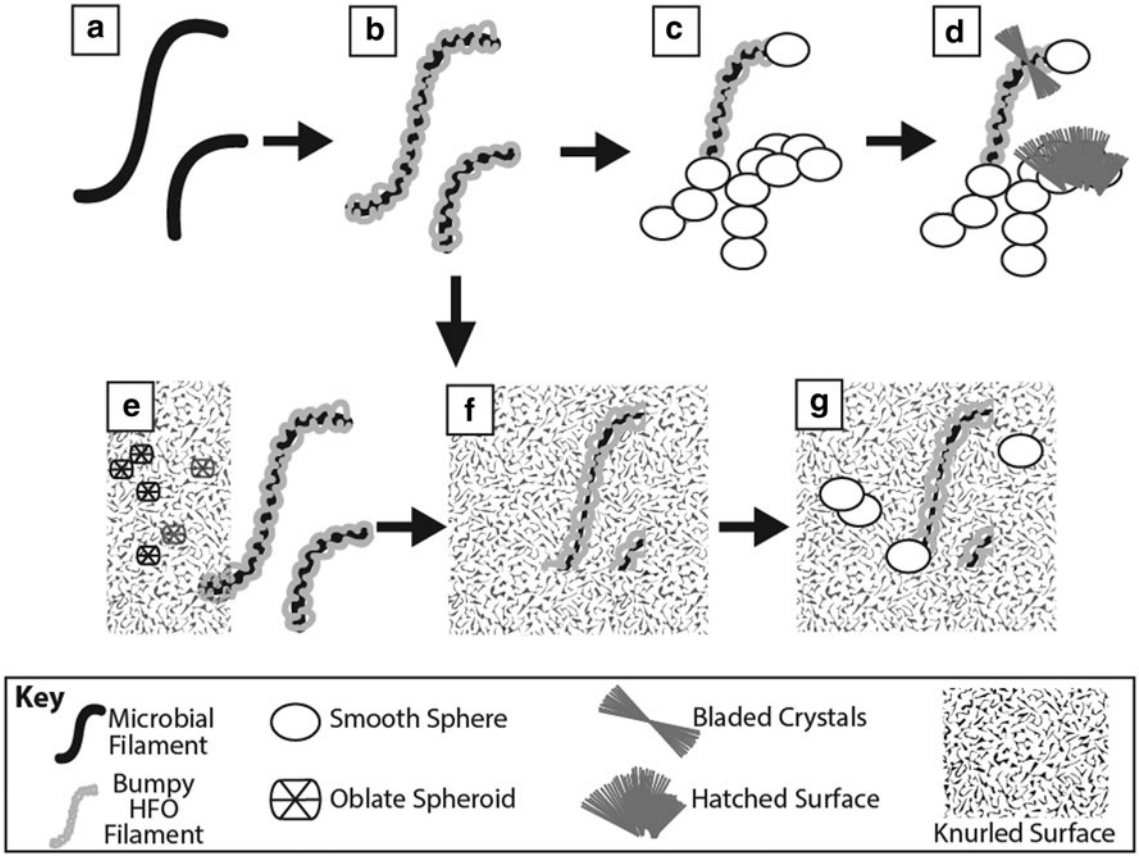

FIG. 12. Bumpy HFO filament formation schematic in the *in situ* gossan. Bare microbial filaments (**a**) are coated with submicrometer HFO particles (**b**). Euhedral HFO minerals coat the filaments and fill in void space, preserving the HFO filament structures. Smooth spheres nucleated on bumpy HFO filaments (**c**). Bladed crystals then nucleated on surfaces, including bumpy HFO filaments, and grew together to form a hatched surface (**d**). Hatched surfaces grew as a front over HFO filaments and smooth spheres. In contrast to the microenvironments with smooth spheres and bladed crystals, bumpy HFO filaments are also preserved by rough oblate spheroids that grew together as knurled surfaces (**e**). These fronts also overgrew bumpy HFO filaments, reducing void space and preserving the filaments (**f**). Smooth spheres then overgrew knurled surfaces and rough oblate spheroids, further reducing void space (**g**).

crystals extending out from the nucleation surface, forming wedge shapes and creating smooth HFO filaments. In some places, extensive HFO precipitate filled in around the HFO filamentous template, suggesting that, after smooth HFO filament formation, another episode of HFO precipitation encapsulated filaments, forming patterned HFO masses. Zones of patterned HFO masses transition abruptly into laminated HFO masses (Fig. 14e). Laminated HFO masses do not contain internal patterns consistent with HFO filaments or encapsulated filaments. This suggests that the HFO precipitated as laminae where there was no preexisting filamentous template for HFO nucleation.

The alternation of HFO textures in remobilized gossan suggests that IO rocks formed in diverse subenvironments. Some of these had filaments to act as nuclei for HFO filaments, whereas others were smoother surfaces. Water flow was rapid based on the speed and flow depth required to transport sand to granules and to align filaments. Thus, shifts in environment related to water availability and flow paths likely played a significant role in variations in gossan texture in contrast to the control exerted by variable permeability in QBR rocks.

5.3. Biosignature potential of HFO filaments

The Iron Mountain HFO filaments provide a good system for evaluating the biosignature potential of HFO filaments because the processes that influence their formation are fairly well constrained. Based on the crystal growth patterns associated with HFO filaments, a filamentous precursor structure existed that was subsequently coated in HFO. Whether or not a filament can be considered to be a biosignature depends on whether the precursor filament was of biotic or abiotic origin. Mineral fibers are the only abiotic fibrous microscale structures known to occur in the Iron Mountain gossan. However, the only fibrous minerals in the Iron Mountain gossan are soluble efflorescent iron-sulfate salts, such as halotrichite group minerals. In general, the solubility of iron-sulfate salts is much higher than that of HFO minerals such as goethite. Also, HFO minerals likely form at pH values above 2 (Nordstrom and Alpers, 1999a). Therefore, solutions saturated in HFO are likely to be undersaturated with respect to iron-sulfate salts. The Fe(III)-saturated waters that precipitate HFO minerals would likely dissolve the iron-sulfate salts before they could be coated in

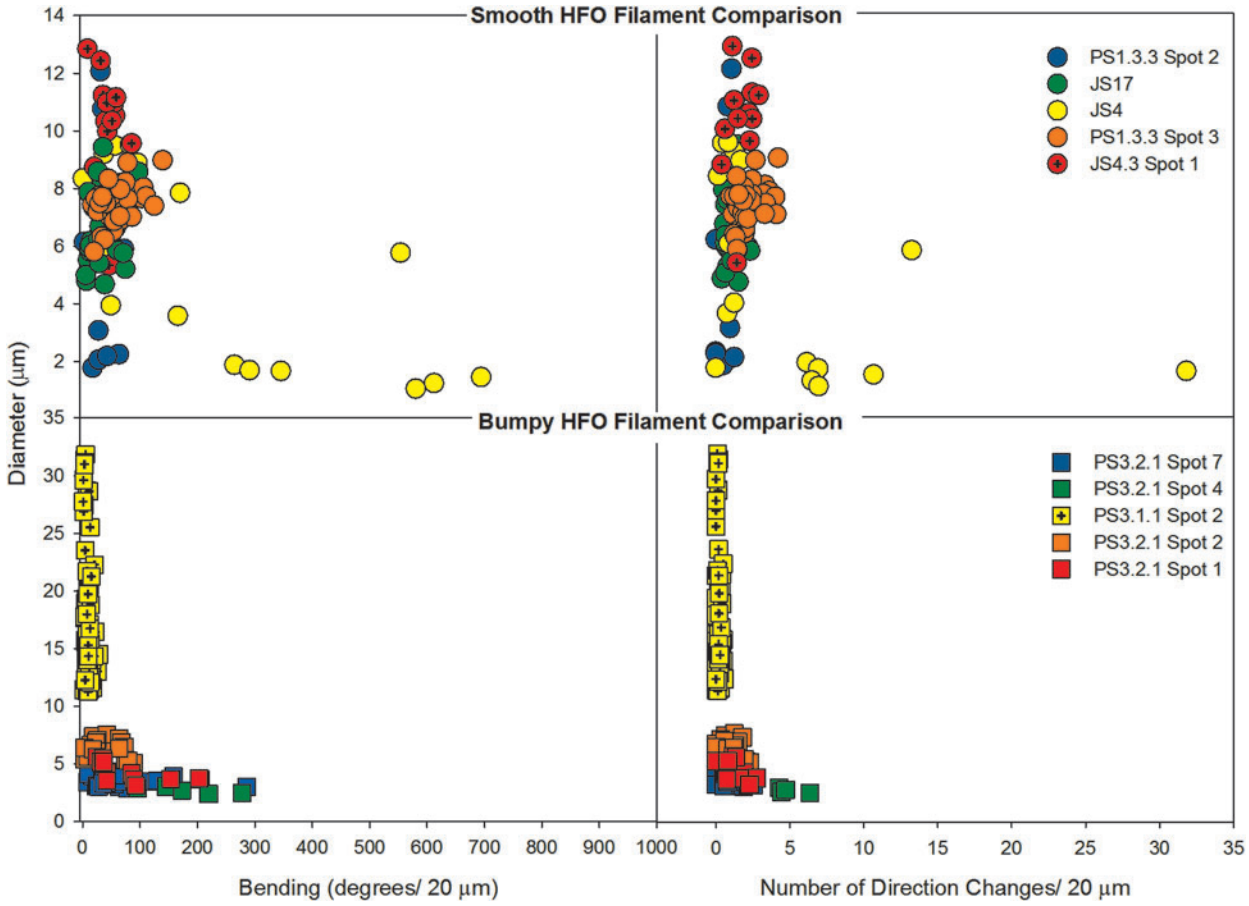

FIG. 13. Diameter versus bending and number of direction changes in smooth (IO) HFO filaments versus bumpy (QBG) HFO filaments. Smooth HFO filaments from all IO samples exhibited a wide range of diameter values (range = ~1 to 13 μm), and all generally overlapped. In comparison, bumpy HFO filament diameters from 4 of 5 sample sites clustered closely together (range = ~2 to 9 μm) based on sample site. Only one QBG sample site (PS3.1.1 Spot 2) exhibited a wide range of diameter values (range = ~11 to 32 μm). Note the different vertical scale bars. (Color graphics available at www.liebertonline.com/ast)

HFO. Thus, iron-sulfate salts are not a likely nucleation site for HFO filament formation, leaving microbial filaments as the most likely nuclei for HFO filaments.

Even though abiotic filamentous precursors for HFO filaments have not been identified, it is instructive to evaluate HFO filaments using established criteria for biosignatures. Characterizing biosignatures in modern rocks may provide insight into how to identify biosignatures in ancient rocks. Because of the importance of rigorously determining whether or not such features are biosignatures, various criteria have been developed to use both morphology and complementary approaches to evaluate the potential biogenicity (Buick, 1990; Hofmann and Farmer, 2000; Banfield *et al.*, 2001; Edwards *et al.*, 2001; Brasier *et al.*, 2002; Garcia-Ruiz *et al.*, 2002; Cady *et al.*, 2003; Schopf *et al.*, 2007; Hofmann *et al.*, 2008). These criteria provide guidelines for assessing the biogenicity of filamentous features in the Iron Mountain gossan (Table 6). They range from evaluations of the environmental context to morphological details and provide an important context for understanding biosignature formation.

(1) *Environmental context*: Many modern environments with active mineral precipitation contain microbial filaments that are overgrown with mineral precipitates, creating a mineral coat around the microbe (Juniper and Fouquet, 1988; Cady and Farmer, 1996; Schultze-Lam *et al.*, 1996; Farmer, 1999; Rasmussen, 2000; Jones *et al.*, 2001; Cady *et al.*, 2003; Kennedy *et al.*, 2004; Little *et al.*, 2004; Fortin and Langley, 2005; Hofmann *et al.*, 2008; Preston *et al.*, 2011). Microbial filaments in the flow path of iron-precipitating fluid in Iron Mountain gossan are likely to be coated in HFO, as pollen grains were. Coated filaments would be preserved as HFO filaments, and coatings of variable thickness would be expected. Thus, the environmental context supports the interpretation that the gossan microbial community can be coated with HFO to form the HFO filaments.

(2) *Presence of extant microbial filaments:* Extant microbial filaments in an active mineral-precipitating environment provide filamentous nucleation sites for mineral precipitation, including HFO mineral precipitation (Cady and Farmer, 1996; Banfield *et al.*, 2001; Parenteau and Cady, 2010; Preston *et al.*, 2011). The presence of bare microbial filaments on the gossan rock exterior in Iron Mountain gossan

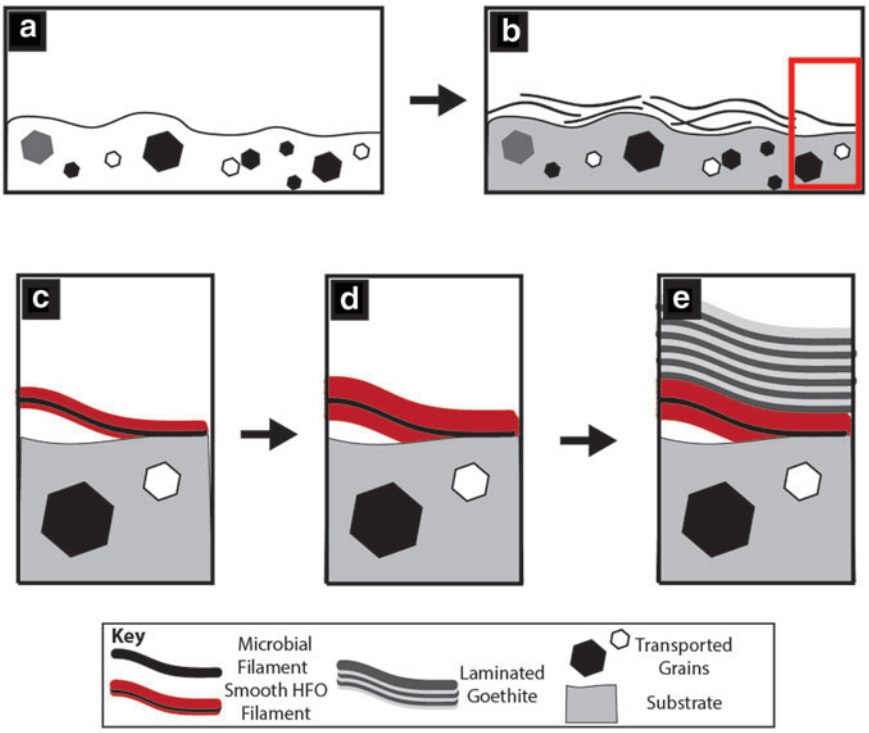

FIG. 14. Smooth HFO filament formation schematic in remobilized iron deposits. (**a**) Mineral grains are transported and lithified. (**b**) Microbial filaments colonize the substrate to form spatially restricted microbial mats. (**c**) With no quartz boxwork to mediate water flow and mineral precipitation, smooth HFO filaments are continually coated with HFO precipitate during wet periods associated with precipitation events. (**d**) HFO filaments are coated to increase in diameter forming generally colloform mineral-coating structures. (**e**) The HFO continues to precipitate, filling in void space around the HFO filaments. Under rapid HFO precipitation conditions and without a filamentous template, HFO precipitates a laminated texture. (Color graphics available at www.liebertonline.com/ast)

indicates that there are modern filamentous microbial communities living in the environment. A similarity in morphology between filamentous microbes present in the samples and mineralized filament lumina provides strong support that the mineralized filaments nucleated on microbial filaments. In the gossan, lumina diameters range from 0.2 to 1.0 μm, which is consistent with some Fe(II)-oxidizing microbial cell diameters (Seeger and Jerez, 1993; Clark and Norris, 1996; Schrenk *et al.*, 1998; Preston *et al.*, 2011). However, the HFO filament lumina are smaller than the microbial filaments identified in the gossan (microbe diameter range 1.3–6.9 μm), requiring either the presence of smaller microbial filaments, shrinkage

Table 6. Comparison of Gossan Biosignatures with Biosignature Criteria from Literature

Criteria	*HFO filaments (This study)*	*Schopf* et al. *(2007)*	*Buick (1990)*	*Hofmann* et al. *(2008)*	*Cady* et al. *(2003)*
Chemical sedimentary/Precipitating environment/Low-temperature assemblage	X	X	X	X	X
Carbonaceous composition/Composed of kerogen		X	X		
In thin section	X		X		X
Differ from surrounding mineral matrix	X				X
Biological morphology					
Distinct cell walls/cellular elaboration		X	X		
Uniform diameters over filament length	X			X	
Cell lumina/core regions	X	X	X	X	
Multiple member population	X	X	X		
Numerous taxa	X	X			
Variable preservation	X	X			
Preserved in 3-D	X	X			
Evidence of filament flexibility, high degrees of bending, many direction changes	X			X	

of the filaments prior to coating, or partial infilling of the lumina. Other microbial organisms identified in prior studies (Table 4) had similar diameters and morphometric values to those described in this study, including eukaryotes (1.5–1.6 μm diameter) from the Iron Mountain mine/Richmond adit (Schrenk *et al.*, 1998; Edwards *et al.*, 1999) and *Leptothrix* sp. microbial mats (1.2–2.2 μm diameter) from iron-dominated aqueous environments (Schieber and Glamoclija, 2007; Florea *et al.*, 2011). The presence of living filaments demonstrates that filamentous microbial communities are present in the gossan rocks and therefore could have provided nucleation sites for HFO minerals, but the difference in lumina diameter raises the possibility that the microbial community that was active during gossan formation differed somewhat from the currently active microbial ecosystem.

(3) *Carbonaceous composition*: A carbonaceous composition and the thermal maturity of organics are an important criterion for interpreting filaments embedded in silica as biosignatures (Buick, 1990; Schopf *et al.*, 2007). However, the preservation of organic carbon in iron oxides is not thermodynamically favored, and organic carbon can decay quickly in oxidizing environments (Cady and Farmer, 1996; Walter *et al.*, 1996, 1998; Farmer, 1999; Sumner, 2004; Hofmann *et al.*, 2008). Although carbon was identified in great abundances as part of extant microbial structures (filamentous plexi, mats of organic filaments, branching filament networks, see Supplementary Material; Fig. 11), it was below detection limits (0.1%) in HFO filaments for the techniques used. Thus, the carbon content of HFO filaments has not been documented, and the amount of carbon present is expected to decrease through time due to decay. Decay can proceed rapidly, within days of cellular death (Bartley, 1996).

(4) *Observable in 3-D in thin section and SEM images:* One of the central criteria for establishing microfossil biogenicity in ancient rocks is the identification of the feature as part of the rock rather than an artifact or younger feature (Buick, 1990). Where mineralized filaments form the bulk of a rock in silica-, carbonate-, or iron-dominated systems, they are clearly indigenous (Walter *et al.*, 1996, 1998; Hofmann and Farmer, 2000). For the gossan samples, the HFO filaments are readily apparent in thin section and SEM, embedded in the minerals and extending into void space within the rock. In some samples, HFO filaments form the bulk of the rock. Thus, they are neither artifacts nor contaminants. Based on cross-cutting relationships with other mineral morphologies, HFO filaments are interpreted to be present early in HFO mineral precipitation. This provides evidence that the filamentous nucleation sites for HFO filaments were part of the original environment in which the rock formed.

(5) *Differ in structural organization from surrounding mineral matrix:* A well-preserved biosignature may be undetectable if it does not differ in composition or structural organization from the surrounding mineral matrix (Cady *et al.*, 2003). The HFO filaments are morphologically distinct from the surrounding mineral morphologies (mineral spheres, bladed structures, etc.), and they require a different nucleation site geometry than surrounding HFO. The geometry of the original filamentous central structure is preserved in the HFO filaments.

(6) *Similarity to biological morphologies:* Although some biological structures mimic abiotic ones, microbial communities have certain characteristics that are rare in abiotic systems. Some of these include evidence of flexibility in filaments, uniform diameters for similar cells, multiple member populations, numerous taxa, distinct cell walls or cellular elaboration, and variable preservation states.

(a) *Evidence of flexibility:* Evidence of filament flexibility in filaments, including high degrees of bending and many direction changes along filaments, is considered a biogenicity indicator (Schopf, 2004; Hofmann *et al.*, 2008). Often, microbial filaments exhibit both high degrees of bending and many direction changes (*e.g.*, Fig. 15), whereas mineral fibers generally have lower values in both parameters (Table 4). Morphological analysis of filaments and fibers from Iron Mountain demonstrates that HFO filaments generally demonstrate high degrees of bending and many direction changes per unit length (Table 4), comparable with microbial filaments (Fig. 15) (Hofmann and Farmer, 2000; Hofmann *et al.*, 2008).

(b) *Uniform diameters:* Uniform filament diameters have been considered a biogenicity indicator in some studies because this is a property of many microbial populations (Schopf, 2004; Hofmann *et al.*, 2008). Microbial filaments frequently have uniform diameters along their length, although some microbial filaments, including fungal hypha, are tapered (Mares *et al.*, 2006; Santelli *et al.*, 2011). The HFO filaments and microbial filaments in Iron Mountain gossan have uniform diameters along their length, similar to results of Hofmann *et al.* (2008).

A central lumen in some HFO filaments may represent the original morphology of the nucleation filament (Hofmann *et al.*, 2008; Williams, 2014a). These lumina are similar to patterns observed during the process of microbial fossilization (Cady and Farmer, 1996; Farmer, 1999; Hofmann *et al.*, 2008; Inskeep *et al.*, 2010), and central lumina in *Leptothrix* sp. sheaths had a similar diameter (0.8–1.0 μm) (Banfield *et al.*, 2001; Gilbert *et al.*, 2005; Furutani *et al.*, 2011) to lumina in the gossan. It is unknown whether *Leptothrix* sp. specifically are present in the gossan. *Leptothrix* are circumneutral iron oxidizers and are found in environments down to pH 6–6.5 (Fleming *et al.*, 2011), similar to the QBG and IO environments at Iron Mountain, which have pH conditions of $\sim$5.5–6. In either case, the presence of central lumina in some Iron Mountain HFO filaments and the consistency in lumina diameter (range = 0.2–1.0 μm) both suggest that

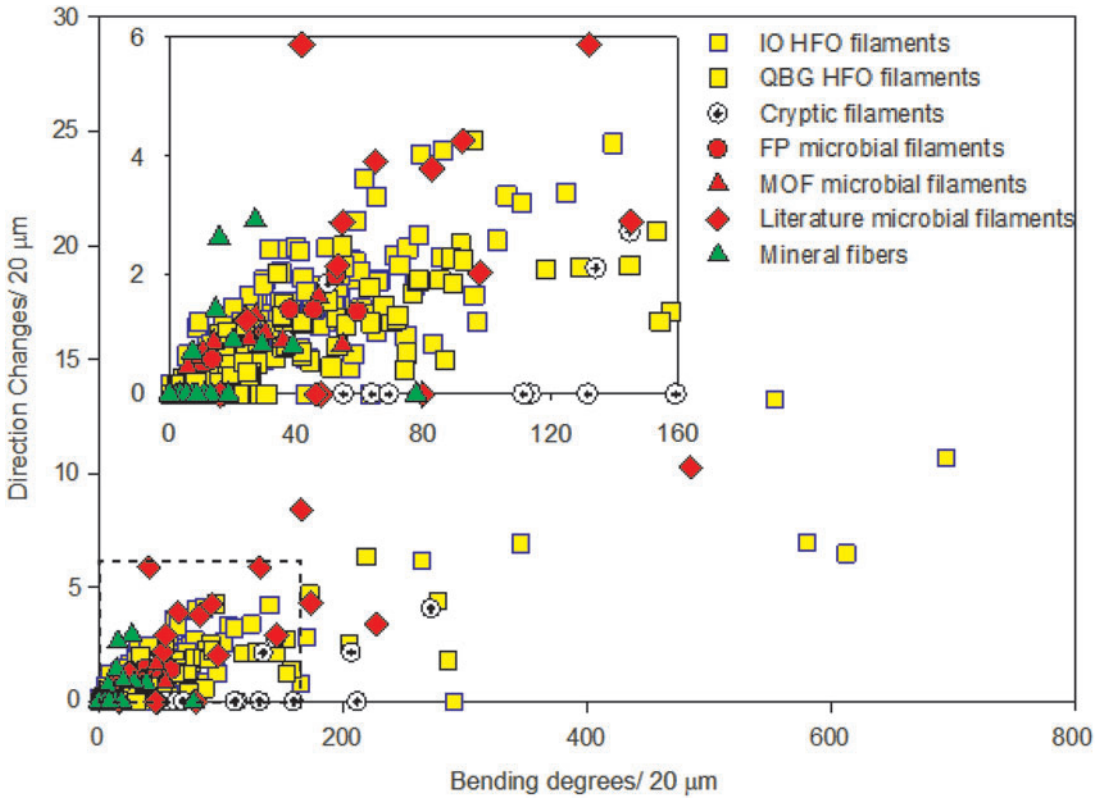

FIG. 15. Comparison of bending (*x* axis) versus number of direction changes (*y* axis) for HFO filaments, cryptic filaments, microbial filaments, and mineral fibers. Microbial filaments, some cryptic filaments, and many HFO filaments exhibit high values in bending and number of direction changes. This demonstrates flexibility and is consistent with morphology parameters for biogenic filaments (Hofmann *et al.*, 2008). Although some HFO filaments can exhibit lower values in bending and number of direction changes, microbial filaments in the gossan exhibit generally similar values, suggesting that the HFO filaments are mineral-coated microbial filaments. (Color graphics available at www.liebertonline.com/ast)

microbial filaments were the nucleation sites for HFO filaments.

In comparison to the uniform HFO filament diameters and lumina, mineral fibers identified in the Iron Mountain gossan (interpreted to be halotrichite group minerals) exhibit a tapered morphology with non-uniform diameters along their length. These tapered mineral morphologies are the only fibrous minerals available to serve as nucleation surfaces for HFO filaments; they would be expected to produce tapered HFO filaments, which were not observed. Based on this, the uniform filament diameters combined with other evidence suggest a biogenic origin for the HFO filaments.

(c) *Multiple member population:* More than one individual of a microbial population should be present and preserved in a given sample to reduce false-positive results in the identification of biogenic structures (Buick, 1990; Schopf *et al.*, 2007). Thousands of individual HFO and microbial filaments have been identified in the Iron Mountain gossan rocks, demonstrating that a significant population was present.

(d) *Numerous taxa:* Microbes almost always grow in multitaxa communities, so some researchers have suggested that if one organism type of a microbial community is preserved, then others should be as well (Schopf *et al.*, 2007). Many different taxa have been identified at Iron Mountain (Williams, 2014b), and three distinct microbial filament types (filamentous plexi, mats of organic filament, and bundled filament networks) in Iron Mountain gossan likely represent different taxa, based on significant differences in morphology. Additionally, the two distinct HFO filament morphologies (bumpy and smooth) are represented in two different mineral-precipitation environments. These environments may have hosted different microbial taxa or communities due to differences in available energy or nutrient resources.

(e) *Distinct cell walls or cellular elaboration:* A primary issue with identifying biosignatures is determining the morphological complexity a feature must possess to preserve enough biological information to be interpreted as microbial in origin (Buick, 1990). Distinct cell walls and cellular elaboration are not preserved in the HFO filaments, and their filamentous structure does not necessitate a biogenic origin because of their relatively low morphological complexity. However, the lack of preserved cell walls or cellular elaboration does not necessarily indicate that the filaments are abiotic. Microbial cells are known to decay and

collapse within several days of cellular death (Bartley, 1996). The absence of fossilized cellular features suggests that their preservation potential is low in this oxidizing environment.

One distinct cellular shape that has been used to support the interpretation of biogenicity is the spiral, as found in the organisms *Gallionella ferruginea* and *Mariprofundus ferrooxidans* (Chan *et al.*, 2011). These organisms represent a freshwater circumneutral iron-oxidizer and a marine iron-oxidizer, respectively. No spiral-shaped features like these were identified in the Iron Mountain gossan, and if they had been, they would have been considered separately from the long, straight filamentous shapes described from this study.

(f) *Variable preservation:* Since microbial communities are in a constant state of flux between living and degrading cells, variable preservation of microbes should be anticipated in the rock record, with a range ''from life-like, to degraded, to markedly decomposed, to biologically nondescript'' (Jones *et al.*, 2001; Schopf *et al.*, 2007; Jones, 2010; Peng and Jones, 2012). In the Iron Mountain gossan, microbial biosignature preservation ranges from bare microbial filaments to HFO filaments with central lumina, to HFO filaments with mineral-filled central cores, and to HFO filaments embedded in mineral masses. Assuming that the central lumina once housed microbial filaments, the lack of preserved central microbial filaments or microbial filaments with bumpy HFO or wedge-shaped crystals nucleated on them suggests that either (1) the HFO filaments did not form recently, and much of the relic organic matter degraded over time, or (2) the HFO filaments formed recently and rapidly, and the filaments quickly degraded in the oxidizing fluid.

Based on these lines of evidence, the HFO filaments are interpreted to be mineral-coated microbial filaments and therefore mineral biosignatures—fundamentally biotically influenced structures. The rarity of bare microbial filaments in these environments makes the recognition of these features as biosignatures all the more crucial to the identification of cryptic biologically influenced structures that lack an organic component.

Even though smooth and bumpy HFO filaments are interpreted as biosignatures, not all mineral filaments can be interpreted as such with confidence. Cryptic filaments were found in PQB samples in association with fibrous efflorescent iron-sulfate crystals. They exhibit diameters, bending, and number of direction changes consistent with microbial filament values. However, they were entwined in fibrous halotrichite group mineral crystals and are a similar average atomic weight as the salt crystals in SEM (Fig. 3d). Thus, cryptic filaments contextually appear to be a newly precipitated sulfate salt mineral even though morphologically they are consistent with mineralized microbial filaments. Therefore, it is difficult to identify them as a mineralogical or microbial structure, leaving their interpretation cryptic.

5.4. Implications for biosignature detection with the Mars Curiosity rover

The acid rock drainage conditions at Iron Mountain make the gossan an appropriate mineralogical and geochemical analogue to certain martian environments (Burns and Fisher, 1990a). By characterizing cryptic physical biosignatures in these analogous environments on Earth, we are better prepared to search for evidence of biosignatures on other rocky planets with *in situ* missions. The Mars Curiosity rover represents an *in situ* mission to characterize a habitable environment on Mars, and it carries an instrument suite capable of detecting some physical and chemical biosignatures. Curiosity landed in Gale Crater, Mars, in August 2012; in winter 2013, the science team demonstrated that at least one past environment on Mars was habitable by known terrestrial microbes (Grotzinger *et al.*, 2014; McLennan *et al.*, 2014; Vaniman *et al.*, 2014). One of the instruments used to characterize this environment was the Mars Hand Lens Imager (MAHLI; Edgett *et al.*, 2012). MAHLI is the highest-resolution camera on the rover, with 13.9 μm/pixel resolution at 2.1 cm working distance (Edgett *et al.*, 2012). At this resolution, an object will need to approach 3 pixels in size to appear discernable, and actual precision (discerning the smallest feature) and accuracy (constraining the distribution of features) are subject to additional constraints (Karunatillake *et al.*, 2013). MAHLI's high-resolution capability is enhanced by its ability to form a Z-stack image, which is one high-resolution image with the full field of view in focus, created from several high-resolution images at multiple focal points (Edgett *et al.*, 2012). These factors make MAHLI one of the most appropriate instruments with which to identify filamentous structures in martian rocks.

The largest individual HFO filaments identified at Iron Mountain are smaller in diameter than the best resolution of MAHLI, but groups of HFO filaments forming matlike structures would be resolvable. To determine the level to which mats of HFO filaments can be resolved, a very-high-resolution (0.8 μm/pixel) Z-stacked image of a smooth HFO filament mat from Iron Mountain was coarsened to MAHLI's highest resolution (Fig. 16) with Adobe Photoshop software. At this resolution, it is challenging to characterize the HFO filament geometries, with errors in filament diameter measurements ranging up to $\times$3.5. However, the overall mat texture is visible and sufficiently suggestive of the presences of biosignatures to support characterization by other rover payload instruments. If such a texture was identified on Mars, the rover instrument suite could be used to couple the distinct texture of HFO filament mats with the characterization of an environment conducive to HFO precipitation. This approach would aid in the investigation of similar features as biosignatures, if present on Mars. With a suite of analyses acquired by the Curiosity instruments to define the geochemical and mineralogical environment, those features could be identified on Mars to be similar to these filaments on Earth, and potentially biogenic. Features such as these could be preserved in iron-rich environments in Curiosity's path.

6. Conclusions

At Iron Mountain, the three dominant rock types of interest for biosignature formation and preservation in the oxidized gossan are PQB, QBG, and IO. PQB rocks are

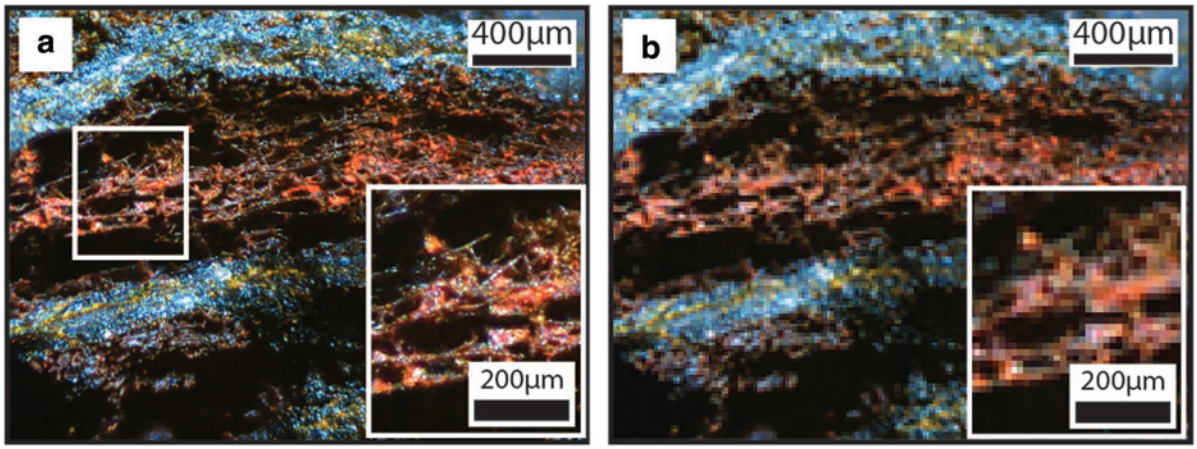

FIG. 16. True color images of HFO filaments at very high resolution versus MAHLI resolution. (**a**) Very-high-resolution (0.8 μm/pixel) Z-stacked image of smooth HFO filament mats. Magnification in inset. (**b**) Same image reduced to MAHLI's highest resolution (13.9 μm/pixel). Magnification in inset. (Color graphics available at www.liebertonline.com/ast)

massive to very fine-grained pyrite surrounded by a white quartz boxwork containing iron-sulfate salts. QBG rocks contain quartz septa, which outline small to medium (<1 to ≥13 mm) pyrite negative pseudomorphs, and HFO minerals are located on the quartz boxwork surface. IO rocks are characterized by a distinct lack of quartz boxwork and only HFO precipitates that form distinct centimeter-scale areas within the regional QBG-type rocks. QBG and IO rocks host HFO filamentous microbial biosignatures; PQB rocks host fibrous efflorescent iron-sulfate salts and cryptic filaments.

Microscale HFO mineral filaments were observed in both QBG and IO rocks. HFO filaments in QBG rocks are hypothesized to have formed when bare microbial filaments are coated with submicrometer HFO particles. The subsequent precipitation of euhedral, subhedral, and anhedral HFO minerals, including smooth spheres, bladed crystals, hatched surfaces, and knurled surfaces, coated the filaments and filled in void space around them, preserving the HFO filament morphology.

Hydrous ferric oxide filaments in IO rocks are hypothesized to have formed from microbial filaments that colonized the iron substrate and formed spatially restricted microbial mats. Microbial filaments were coated in HFO minerals forming gently oriented to strongly oriented smooth HFO filaments. These HFO filaments were overgrown by subsequent laminated and patterned iron mineral precipitation that filled in around preexisting HFO filaments and did not preserve the microbial template. Smooth HFO filament morphology distributions (bending and number of direction changes) demonstrate that all the HFO filaments in each IO microenvironment occupy a broad range of values for bending and number of direction changes, and that samples from different IO rocks all generally overlapped in those values. This trend suggests that the processes that formed these HFO filaments, which are hypothesized here to be the mobilization and precipitation of HFO and flow across the surface of the rock, were the dominant controls on filament formation.

The HFO filaments fulfill previously defined biosignature criteria by Buick (1990), Schopf *et al.* (2007), Cady *et al.* (2003), and Hofmann *et al.* (2008), which include environmental context, carbonaceous composition, features observable in thin section and SEM, difference in structural organization from surrounding mineral matrix, and a biological morphology. HFO filaments are one of the first mineral morphologies present, based on cross-cutting relationships with other mineral morphologies. They were present early in HFO mineral precipitation, providing evidence that the nucleation site had to first be present for the other mineral morphologies to precipitate on it. Additionally, the diameter consistency in central filament lumina suggests that a filamentous structure of relatively consistent diameter, likely a microbial filament, was present inside the HFO filament and likely served as a nucleation site for mineral precipitation. The presence of bare microbial filaments on the rock exterior indicates that there are currently filamentous microbial communities on the rock surface. Morphometric analysis shows that HFO filaments generally demonstrate high degrees of bending and number of direction changes per unit length, comparable with microbial filaments. Mineral fibers generally have lower values in both parameters.

Identification of most mineral filaments as terrestrial biosignatures allows us to recognize similar microbial fabrics in environments beyond Earth, such as on Mars. Individual HFO filaments are below MAHLI camera resolution; however, sinuous HFO filaments that form matlike textures are resolvable. With a suite of analyses acquired by the Curiosity rover instruments to define the geochemical and mineralogical environment, those features could be identified on Mars to be similar to these filaments on Earth, and potentially biogenic. These features could be preserved in a variety of acid-sulfate weathered, iron-rich environments in Curiosity's path to Mt. Sharp in Gale Crater.

Acknowledgments

This work is supported by NASA Headquarters under the NASA Earth and Space Science Fellowship Program Grant NNX11AQ51H and by the UCD Geology department Durrell Funds. Thanks to Iron Mountain operations, USEPA, USGS, T. Arman and IMM Inc., J. Peterson and T. Mackey

for field assistance, A. Phan and D. McKim for assistance with filament morphology measurements, R. Southard, F. Hayes and I. Delusina for laboratory assistance. We thank Robert Bowell, Jane Hammarstrom, and two anonymous reviewers for their comments, which helped strengthen the manuscript. Any use of trade, firm, or product names is for descriptive purposes only and does not imply endorsement by the US Government.

Author Disclosure Statement

No competing financial interests exist.

References

Abdel-Aal, E.A. and Farghaly, F.E. (2007) Preparation of silver powders in micron size from used photographic films via leaching–cementation technique. *Powder Technol* 178: 51–55.

Albers, J.P. (1985) Geology of the Brick Flat massive sulfide body, Iron Mountain cluster, West Shasta District, California. *Econ Geol* 80:2092–2099.

Albers, J.P. and Bain, J.H. (1985) Regional setting and new information on some critical geologic features of the West Shasta District, California. *Econ Geol* 80:2072–2091.

Alpers, C.N., Nordstrom, D.K., Verosub, K.L., and Helm, C.M. (1999) Paleomagnetic reversals in Iron Mountain gossan provides limits on long-term premining metal flux rates. In *Geological Society of America Abstracts with Programs*, Vol. 31, Geological Society of America, Boulder, CO, p A-33.

Alpers, C.N., Nordstrom, D.K., and Spitzley, J. (2003) Extreme acid mine drainage from a pyritic massive sulfide deposit: the Iron Mountain endmember. In *Environmental Aspects of Mine Wastes*, edited by J.L. Jambor, D.W. Blowes, and A.I.M. Ritchie, Short Course Notes 31, Mineralogical Association of Canada, Ottawa, pp 407–430.

Baker, B.J. and Banfield, J.F. (2003) Microbial communities in acid mine drainage. *FEMS Microbiol Ecol* 44:139–152.

Banfield, J.F., Moreau, J.W., Chan, C.S., Welch, S.A., and Little, B. (2001) Mineralogic biosignatures and the search for life on Mars. *Astrobiology* 1:447–465.

Barrie, C.T. and Hannington, M.D. (2000) Classification of volcanic-hosted massive sulfide deposits based on host-rock composition. In *Volcanic-Associated Massive Sulfide Deposits: Processes and Examples in Modern and Ancient Settings*, edited by C.T. Barrie and M.D. Hannington, Reviews in Economic Geology 8, Society of Economic Geologists, Littleton, CO, pp 1–11.

Bartley, J.K. (1996) Actualistic taphonomy of cyanobacteria: implications for the Precambrian fossil record. *Palaios* 11:571–586.

Blanchard, R. (1968) *Interpretation of Leached Outcrops*, Nevada Bureau of Mines Bulletin 66, MacKay School of Mines, University of Nevada, Reno.

Brasier, M.D., Green, O.R., Jephcoat, A.P., Kleppe, A.K., Van Kranendonk, M.J., Lindsay, J.F., Steele, A., and Grassineau, N.V. (2002) Questioning the evidence for Earth's oldest fossils. *Nature* 416:76–81.

Buick, R. (1990) Microfossil recognition in Archean rocks: an appraisal of spheroids and filaments from a 3500 m.y. old chert-barite unit at North Pole, Western Australia. *Palaios* 5:441–459.

Burns, R.G. (1987) Gossans on Mars: spectral features attributed to jarosite [abstract 1072]. In *Eighteenth Lunar and Planetary Science Conference*, Lunar and Planetary Institute, Houston.

Burns, R.G. and Fisher, D.S. (1990a) Evolution of sulfide mineralization on Mars. *J Geophys Res* 95:14169–14173.

Burns, R.G. and Fisher, D.S. (1990b) Iron-sulfur mineralogy of Mars: magmatic evolution and chemical weathering products. *J Geophys Res* 95:14415–14421.

Cady, S.L. and Farmer, J.D. (1996) Fossilization processes in siliceous thermal springs: trends in preservation along the thermal gradient. In *Evolution of Hydrothermal Ecosystems on Earth (and Mars?)*, Ciba Foundation Symposium 202, edited by G.R. Bock and J.A. Goode, Wiley and Sons, Chichester, UK, pp 150–173.

Cady, S.L., Farmer, J.D., Grotzinger, J.P., Schopf, J.W., and Steele, A. (2003) Morphological biosignatures and the search for life on Mars. *Astrobiology* 3:351–368.

Cavanagh, P.D., Bish, D.L., Blake, D.F., Vaniman, D.T., Morris, R.V., Ming, D.W., Rampe, E.B., Achilles, C.N., Chipera, S.J., Treiman, A.H., Downs, R.T., Morrison, S.M., Fendrich, K.V., Yen, A.S., Grotzinger, J.P., Crisp, J.A., Bristow, T.F., Sarrazin, P.C., Farmer, J.D., Des Marais, D.J., Stolper, E.M., Morookian, J.M., Wilson, M.A., Spanovich, N., and Anderson, R.C. (2015) Confidence Hills mineralogy and CheMin results from base of Mt. Sharp, Pahrump Hills, Gale Crater, Mars [abstract 2735]. In *46th Lunar and Planetary Science Conference*, Lunar and Planetary Institute, Houston.

Chan, C.S., Fakra, S.C., Emerson, D., Fleming, E.J., and Edwards, K.J. (2011) Lithotrophic iron-oxidizing bacteria produce organic stalks to control mineral growth: implications for biosignature formation. *ISME J* 5:717–727.

Clark, D.A. and Norris, P.R. (1996) *Acidimicrobium ferrooxidans* gen. nov., sp. nov.: mixed-culture ferrous iron oxidation with *Sulfobacillus* species. *Microbiology* 142:785–790.

Downs, R.T. (2006) The RRUFF Project: an integrated study of the chemistry, crystallography, Raman and infrared spectroscopy of minerals. In *Program and Abstracts of the 19th General Meeting of the International Mineralogical Association in Kobe, Japan*, O03–13.

Edgett, K.S., Yingst, R.A., Ravine, M.A., Caplinger, M.A., Maki, J.N., Ghaemi, F.T., Schaffner, J.A., Bell, J.F., III, Edwards, L.J., Herkenhoff, K.E., Heydari, E., Kah, L.C., Lemmon, M.T., Minitti, M.E., Olson, T.S., Parker, T.J., Rowland, S.K., Schieber, J., Sullivan, R.J., Sumner, D.Y., Thomas, P.C., Jensen, E.H., Simmonds, J.J., Sengstacken, A.J., Willson, R.G., and Goetz, W. (2012) Curiosity's Mars Hand Lens Imager (MAHLI) investigation. *Space Sci Rev* 170:259–317.

Edwards, K.J., Gihring, T.M., and Banfield, J.F. (1999) Seasonal variations in microbial populations and environmental conditions in an extreme acid mine drainage environment. *Appl Environ Microbiol* 65:3627–3632.

Edwards, K.J., Hu, B., Hamers, R.J., and Banfield, J.F. (2001) A new look at microbial leaching patterns on sulfide minerals. *FEMS Microbiol Ecol* 34:197–206.

Farmer, J.D. (1999) Taphonomic modes in microbial fossilization. In *Size Limits of Very Small Microorganisms: Proceedings of a Workshop*, Space Studies Board, National Research Council, National Academies Press, Washington, DC, pp 94–102.

Farmer, J.D., Bish, D.L., Blake, D.F., Ming, D.W., Morris, R.V., Vaniman, D.T., Achilles, C.N., Anderson, R.C., Bristow, T.F., Cavanagh, P.D., Chipera, S.J., Crisp, J.A., Downs, R.T., Des Marais, D.J., Fendrich, K.V., Grotzinger, J., Mor-

ookian, J.M., Morrison, S.M., Rampe, E.B., Treiman, A.H., Sarrazin, P.C., Spanovich, N., Stolper, E.M., and Yen, A.S. (2015) Iron and sulfur mineralogy of Gale Crater sediments signals changes in habitable conditions during diagenesis [abstract 7267]. In *Astrobiology Science Conference 2015*, Lunar and Planetary Institute, Houston.

Fleming, E.J., Langdon, A.E., Martinez-Garcia, M., Stepanauskas, R., Poulton, N.J., Masland, E.D.P., and Emerson, D. (2011) What's new is old: resolving the identity of *Leptothrix ochracea* using single cell genomics, pyrosequencing and FISH. *PLoS One* 6:e17769.

Florea, L.J., Noe-Stinson, C.L., Brewer, J., Fowler, R., Kearns, J.B., and Greco, A.M. (2011) Iron oxide and calcite associated with *Leptothrix* sp. biofilms within an estavelle in the upper Floridan aquifer. *Int J Speleol* 40:205–219.

Fortin, D. and Langley, S. (2005) Formation and occurrence of biogenic iron-rich minerals. *Earth-Science Reviews* 72: 1–19.

Fortin, D., Ferris, F.G., and Beveridge, T.J. (1997) Surface mediated mineral development by bacteria. In *Reviews in Mineralogy 35: Geomicrobiology: Interaction Between Microbes and Minerals*, edited by J.F. Banfield and K.H. Nealson, Mineralogical Society of America, Washington, DC, pp 161–180.

Fraeman, A.A., Arvidson, R.E., Catalano, J.G., Grotzinger, J.P., Morris, R.V., Murchie, S.L., Stack, K.M., Humm, D.C., McGovern, J.A., Seelos, F.P., Seelos, K.D., and Viviano, C.E. (2013) A hematite-bearing layer in Gale Crater, Mars: mapping and implications for past aqueous conditions. *Geology* 41:1103–1106.

Franklin, J.M., Hannington, M.D., Jonasson, I.R., and Barrie, C.T. (1998) Arc-related volcanogenic massive sulphide deposits. In *Metallogeny of Volcanic Arcs*, edited by D.V. Lefebure, British Columbia Geological Survey Short Course Notes Open File 1998-5, British Columbia Geological Survey, Victoria, Canada, Section N.

Fru, E.C., Ivarsson, M., Kilias, S.P., Bengtson, S., Belivanova, V., Marone, F., Fortin, D., Broman, C., and Stampanoni, M. (2013) Fossilized iron bacteria reveal a pathway to the biological origin of banded iron formation. *Nat Commun* 4, doi:10.1038/ncomms3050.

Furutani, M., Suzuki, T., Ishihara, H., Hashimoto, H., Kunoh, H., and Takada, J. (2011) Assemblage of bacterial saccharic microfibrils in sheath skeleton formed by cultured *Leptothrix* sp. strain OUMS1. *Journal of Marine Science: Research & Development* Special Issue 5, doi:10.4172/2155-9910.S5-001.

Garcia-Ruiz, J.M., Carnerup, A., Christy, A.G., Welham, N.J., and Hyde, S.T. (2002) Morphology: an ambiguous indicator of biogenicity. *Astrobiology* 2:353–369.

Gilbert, P.U.P.A., Abrecht, M., and Frazer, B.H. (2005) The organic-mineral interface in biominerals. *Reviews in Mineralogy and Geochemistry* 59:157–185.

Gomes, M.E.P. and Favas, P.J.C. (2006) Mineralogical controls on mine drainage of the abandoned Ervedosa tin mine in north-eastern Portugal. *Appl Geochem* 21:1322–1334.

Grotzinger, J.P., Sumner, D.Y., Kah, L.C., Stack, K., Gupta, S., Edgar, L., Rubin, D., Lewis, K., Schieber, J., Mangold, N., Milliken, R., Conrad, P.G., Des Marais, D., Farmer, J., Siebach, K., Calef, F., III, Hurowitz, J., McLennan, S.M., Ming, D., Vaniman, D., Crisp, J., Vasavada, A., Edgett, K.S., Malin, M., Blake, D., Gellert, R., Mahaffy, P., Wiens, R.C., Maurice, S., Grant, J.A., Wilson, S., Anderson, R.C., Beegle, L., Arvidson, R., Hallet, B., Sletten, R.S., Rice, M., Bell, J., III, Griffes, J., Ehlmann, B., Anderson, R.B., Bristow, T.F., Dietrich, W.E., Dromart, G., Eigenbrode, J., Fraeman, A., Hardgrove, C., Herkenhoff, K., Jandura, L., Kocurek, G., Lee, S., Leshin, L.A., Leveille, R., Limonadi, D., Maki, J., McCloskey, S., Meyer, M., Minitti, M., Newsom, H., Oehler, D., Okon, A., Palucis, M., Parker, T., Rowland, S., Schmidt, M., Squyres, S., Steele, A., Stolper, E., Summons, R., Treiman, A., Williams, R., and Yingst, A. (2014) Habitable fluvio-lacustrine environment at Yellowknife Bay, Gale Crater, Mars. *Science Express* 343, doi:10.1126/science.1242777.

Gumaelius, L., Magnusson, G., Pettersson, B., and Dalhammar, G. (2001) *Comamonas denitrificans* sp. nov., an efficient denitrifying bacterium isolated from activated sludge. *Int J Syst Evol Microbiol* 51:999–1006.

Hammarstrom, J.M., Seal, R.R., II, Meier, A.L., and Kornfield, J.M. (2005) Secondary sulfate minerals associated with acid drainage in the eastern US: recycling of metals and acidity in surficial environments. *Chem Geol* 215:407–431.

Hofmann, B.A. and Farmer, J.D. (2000) Filamentous fabrics in low-temperature mineral assemblages: are they fossil biomarkers? Implications for the search for a subsurface fossil record on the early Earth and Mars. *Planet Space Sci* 48:1077–1086.

Hofmann, B.A., Farmer, J.D., von Blanckenburg, F., and Fallick, A.E. (2008) Subsurface filamentous fabrics: an evaluation of origins based on morphological and geochemical criteria, with implications for exopaleontology. *Astrobiology* 8:87–117.

Inskeep, W.P., Rusch, D.B., Jay, Z.J., Herrgard, M.J., Kozubal, M.A., Richardson, T.H., Macur, R.E., Hamamura, N., Jennings, R.D., Fouke, B.W., Reysenbach, A.-L., Roberto, F., Young, M., Schwartz, A., Boyd, E.S., Badger, J.H., Mathur, E.J., Ortmann, A.C., Bateson, M., Geesey, G., and Frazier, M. (2010) Metagenomes from high-temperature chemotrophic systems reveal geochemical controls on microbial community structure and function. *PLoS One* 5:e9773.

Jamieson, H.E., Robinson, C., Alpers, C.N., McCleskeym, R.B., Nordstrom, D.K., and Peterson, R.C. (2005) Major and trace element composition of copoapite-group minerals and coexisting water from the Richmond mine, Iron Mountain, California. *Chem Geol* 215:387–405.

Jones, B. (2010) Speleothems in a wave-cut notch, Cayman Brac, British West Indies: the integrated product of subaerial precipitation, dissolution, and microbes. *Sedimentary Geology* 232:15–34.

Jones, B., Renaut, R.W., and Rosen, M.R. (2001) Biogenicity of gold- and silver-bearing siliceous sinters forming in hot (75C) anaerobic spring-waters of Champagne Pool, Waiotapu, North Island, New Zealand. *J Geol Soc London* 158: 895–911.

Juniper, S.K. and Fouquet, Y. (1988) Filamentous iron-silica deposits from modern and ancient hydrothermal sites. *Can Mineral* 26:859–869.

Karunatillake, S., Squyres, S.W., Gasnault, O., Keller, J.M., Janes, D.M., Boynton, W.V., and Finch, M.J. (2011) Recipes for spatial statistics with global datasets: a martian case study. *J Sci Comput* 46:439–451.

Karunatillake, S., McLennan, S.M., Herkenhoff, K.E., Husch, J.M., Hardgrove, C., and Skok, J.R. (2013) A martian case study of segmenting images automatically for granulometry and sedimentology, part 1: algorithm. *Icarus* 229:400–407.

Karunatillake, S., Wray, J.J., Gasnault, O., McLennan, S.M., Rogers, A.D., Squyres, S.W., Boynton, W.V., Skok, J.R., Ojha, L., and Olsen, N. (2014) Sulfates hydrating bulk soil in

the martian low and middle latitudes. *Geophys Res Lett* 41:7987–7996.

Kennedy, C.B., Scott, S.D., and Ferris, F.G. (2004) Hydrothermal phase stabilization of 2-line ferrihydrite by bacteria. *Chem Geol* 212:269–277.

Kinkel, A.R., Jr., Hall, W.E., and Albers, J.P. (1956) *Geology and Base Metal Deposits of West Shasta Copper-Zinc District, Shasta County, California*, USGS Professional Paper 285, United States Government Printing Office, Washington, DC.

Lane, M.D., Bishop, J.L., Dyar, M.D., Hiroi, T., Mertzman, S.A., Bish, D.L., King, P.L., and Rogers, A.D. (2015) Mid-infrared emission spectroscopy and visible/near-infrared reflectance spectroscopy of Fe-sulfate minerals. *Am Mineral* 100:66–82.

Little, C.T.S., Glynn, S.E.J., and Mills, R.A. (2004) Four-hundred-and-ninety-million-year record of bacteriogenic iron oxide precipitation at sea-floor hydrothermal vents. *Geomicrobiology J* 21:415–429.

Majzlan, J., Navrotsky, A., McCleskey, R.B., and Alpers, C.N. (2006) Thermodynamic properties and crystal structure refinement of ferricopiapite, coquimbite, rhomboclase, and $Fe_2(SO_4)_3(H_2O)_5$. *European Journal of Mineralogy* 18:175–186.

Mares, D., Romagnoli, C., Andreotti, E., Forlani, G., Guccione, S., and Vicentini, C.B. (2006) Emerging antifungal azoles and effects on *Magnaporthe grisea*. *Mycol Res* 110:686–696.

McAdam, A.C., Archer, P.D., Jr., Sutter, B., Franz, H.B., Eigenbrode, J.L., Ming, D.W., Morris, R.V., Niles, P.B., Stern, J.C., Freissinet, C., Glavin, D.P., Atreya, S.K., Bish, D.L., Blake, D.F., Mahaffy, P.R., Navarro-Gonzalez, R., McKay, C.P., and Wilhelm, M.B. (2015) Major volatiles from MSL SAM evolved gas analyses: Yellowknife Bay through lower Mount Sharp [abstract 2323]. In *46th Lunar and Planetary Science Conference*, Lunar and Planetary Institute, Houston.

McLennan, S.M., Anderson, R.B., Bell, J.F., Bridges, J.C., Calef, F., Campbell, J.L., Clark, B.C., Clegg, S., Conrad, P., Cousin, A., Des Marais, D.J., Dromart, G., Dyar, M.D., Edgar, L.A., Ehlmann, B.L., Fabre, C., Forni, O., Gasnault, O., Gellert, R., Gordon, S., Grant, J.A., Grotzinger, J.P., Gupta, S., Herkenhoff, K.E., Hurowitz, J.A., King, P.L., Le Mouélic, S., Leshin, L.A., Léveillé, R., Lewis, K.W., Mangold, N., Maurice, S., Ming, D.W., Morris, R.V., Nachon, M., Newsom, H.E., Ollila, A.M., Perrett, G.M., Rice, M.S., Schmidt, M.E., Schwenzer, S.P., Stack, K., Stolper, E.M., Sumner, D.Y., Treiman, A.H., VanBommel, S., Vaniman, D.T., Vasavada, A., Wiens, R.C., Yingst, R.A.; the MSL Science Team. (2014) Elemental geochemistry of sedimentary rocks at Yellowknife Bay, Gale Crater, Mars. *Science* 343, doi:10.1126/science.1244734.

Murgida, D.H. and Hildebrandt, P. (2008) Disentangling interfacial redox processes of proteins by SERR spectroscopy. *Chem Soc Rev* 37:937–945.

Nordstrom, D.K. (2003) Effects of microbiological and geochemical interactions in mine drainage In *Environmental Aspects of Mine Wastes*, edited by J.L. Jambor, D.W. Blowes, and A.I.M. Ritchie, Short Course Notes 31, Mineralogical Association of Canada, Ottawa, pp 227–238.

Nordstrom, D.K. and Alpers, C.N. (1999a) Geochemistry of acid mine waters. In *The Environmental Geochemistry of Mineral Deposits. Part A. Processes, Methods, and Health Issues,* Reviews in Economic Geology 6A, edited by G.S. Plumlee and M.J. Logsdon, Society of Economic Geologists, Littleton, CO, pp 133–160.

Nordstrom, D.K. and Alpers, C.N. (1999b) Negative pH, efflorescent mineralogy, and consequences for environmental restoration at the Iron Mountain Superfund site, California. *Proc Natl Acad Sci USA* 96:3455–3462.

Panneerselvam, A., Malik, M.A., O'Brien, P., and Raftery, J. (2008) The CVD of silver sulfide and silver thin films from a homoleptic crystalline single-source precursor. *Journal of Materials Chemistry* 18:3264–3269.

Parenteau, M.N. and Cady, S.L. (2010) Microbial biosignatures in iron-mineralized phototrophic mats at Chocolate Pots hot springs, Yellowstone National Park, United States. *Palaios* 25:97–111.

Peng, X. and Jones, B. (2012) Rapid precipitation of silica (opal-A) disguises evidence of biogenicity in high-temperature geothermal deposits: case study from Dagunguo hot spring, China. *Sedimentary Geology* 257–260:45–62.

Peterson, R.C., Williamson, M.-C., and Rainbird, R.H. (2014) Gossan Hill, Victoria Island, Northwest Territories: an analogue for mine waste reactions within permafrost and implication for the subsurface mineralogy of Mars. *Earth Planet Sci Lett* 400:88–93.

Preston, L.J., Shuster, J., Fernandez-Remolar, D., Banerjee, N.R., Osinski, G.R., and Southam, G. (2011) The preservation and degradation of filamentous bacteria and biomolecules within iron oxide deposits at Río Tinto, Spain. *Geobiology* 9:233–249.

Rasmussen, B. (2000) Filamentous microfossils in a 3,235-million-year-old volcanogenic massive sulphide deposit. *Nature* 405:676–679.

Santelli, C.M., Webb, S.M., Dohnalkova, A.C., and Hansel, C.M. (2011) Diversity of Mn oxides produced by Mn(II)-oxidizing fungi. *Geochim Cosmochim Acta* 75:2762–2776.

Schieber, J. and Glamoclija, M. (2007) Microbial mats built by iron bacteria: a modern example from southern Indiana. In *Atlas of Microbial Mat Features Preserved within the Clastic Rock Record*, edited by J. Schieber, P.K. Bose, P.G. Eriksson, S. Banerjee, S. Sarkar, W. Altermann, and O. Catuneanu, Elsevier, Amsterdam, pp 233–244.

Schopf, J.W. (2004) Earth's earliest biosphere: status of the hunt. In *The Precambrian Earth: Tempos and Events*, edited by P.G. Eriksson, W. Altermann, D.W. Nelson, W.U. Mueller, and O. Catuneanu, Elsevier, New York, pp 516–539.

Schopf, J.W., Kudryavtsev, A.B., Czaja, A.D., and Tripathi, A.B. (2007) Evidence of Archean life: stromatolites and microfossils. *Precambrian Res* 158:141–155.

Schrenk, M.O., Edwards, K.J., Goodman, R.M., Hamers, R.J., and Banfield, J.F. (1998) Distribution of *Thiobacillus ferrooxidans* and *Leptospirillum ferrooxidans:* implications for generation of acid mine drainage. *Science* 279:1519–1522.

Schultze-Lam, S., Fortin, D., Davis, B., and Beveridge, T.J. (1996) Mineralization of bacterial surfaces. *Chem Geol* 132:171–181.

Seeger, M. and Jerez, C. (1993) Phosphate starvation-induced changes in *Thiobacillus ferrooxidans*. *FEMS Microbiol Lett* 108:35–42.

Sobron, P. and Alpers, C.N. (2013) Raman spectroscopy of efflorescent sulfate salts from Iron Mountain mine superfund site, California. *Astrobiology* 13:270–278.

Squyres, S.W., Grotzinger, J.P., Arvidson, R.E., Bell, J.F., III, Calvin, W., Christensen, P.R., Clark, B.C., Crisp, J.A., Farrand, W.H., Herkenhoff, K.E., Johnson, J.R., Klingelhofer, G., Knoll, A.H., McLennan, S.M., McSween, H.Y., Jr., Morris, R.V., Rice, J.W., Jr., Rieder, R., and Soderblom, L.A. (2004) *In situ* evidence for an ancient aqueous environment at Meridiana Planum, Mars. *Science* 306:1709–1714.

Sumner, D.Y. (2004) Poor preservation potential of organics in Meridiani Planum hematite-bearing sedimentary rocks. *J Geophys Res* 109, doi:10.1029/2004JE002321.

Taylor, R.G. (2011) *Gossans and Leached Cappings: Field Assessment*, Springer-Verlag, Berlin.

Vaniman, D.T., Bish, D.L., Ming, D.W., Bristow, T.F., Morris, R.V., Blake, D.F., Chipera, S.J., Morrison, S.M., Treiman, A.H., Rampe, E.B., Rice, M., Achilles, C.N., Grotzinger, J., McLennan, S.M., Williams, J., Bell, J., Newsom, H., Downs, R.T., Maurice, S., Sarrazin, P., Yen, A.S., Morookian, J.M., Farmer, J.D., Stack, K., Milliken, R.E., Ehlmann, B., Sumner, D.Y., Berger, G., Crisp, J.A., Hurowitz, J.A., Anderson, R., Des Marais, D., Stolper, E.M., Edgett, K.S., Gupta, S., Spanovich, N., and the MSL Science Team. (2014) Mineralogy of a mudstone at Yellowknife Bay, Gale Crater, Mars. *Science* 343, doi:10.1126/science.1243480.

Velasco, F., Herrero, J.M., Suárez, S., Yusta, I., Alvaro, A., and Tornos, F. (2013) Supergene features and evolution of gossans capping massive sulphide deposits in the Iberian Pyrite Belt. *Ore Geology Reviews* 53:181–203.

Walter, M.R., Des Marais, D.J., Farmer, J.D., and Hinman, N.W. (1996) Lithofacies and biofacies of Mid-Paleozoic thermal spring deposits in the Drummond Basin, Queensland, Australia. *Palaios* 11:497–518.

Walter, M.R., Mcloughlin, S., Drinnan, A.N., and Farmer, J.D. (1998) Palaeontology of Devonian thermal spring deposits, Drummond Basin, Australia. *Alcheringa: An Australasian Journal of Palaeontology* 22:285–314.

West, L., McGown, D.J., Onstott, T.C., Morris, R.V., Suchecki, P., and Pratt, L.M. (2009) High Lake gossan deposit: an Arctic analogue for ancient martian surficial processes? *Planet Space Sci* 57:1302–1311.

Williams, A.J. (2014a) Microbial biosignature preservation at Iron Mountain, California. PhD thesis, University of California, Davis, CA, Chapter 2.

Williams, A.J. (2014b) Microbial biosignature preservation at Iron Mountain, California. PhD thesis, University of California, Davis, CA, Chapter 3.

Address correspondence to:
Amy J. Williams
NASA Goddard Space Flight Center
8800 Greenbelt Road
Greenbelt, MD 20771

E-mail: amy.j.williams@nasa.gov

Submitted 1 October 2014
Accepted 7 June 2015

Abbreviations Used

BSE = backscatter electron
EDS = energy-dispersive spectroscopy
ESEM = environmental scanning electron microscopy
FEG = field emission gun
HFO = hydrous ferric oxide
IO = iron-only
MAHLI = Mars Hand Lens Imager
PQB = pyrite and quartz boxwork
QBG = HFO and quartz boxwork gossan
SE = secondary electron
SEM = scanning electron microscopy
UC = University of California
XRD = X-ray diffraction